Boron Neutron Capture Therapy
Treatment Planning Improvements

by

John Timothy Goorley

B.S. Nuclear Engineering
B.S. Radiological Health Engineering
Texas A&M University (1996)

Submitted to the Department of Nuclear Engineering
in partial fulfillment of the requirements for the degree of

Masters of Science in Nuclear Engineering

at the

Massachusetts Institute of Technology

June 1998

Author ....
Nuclear Engineering Department
May 7, 1998

Certified by ....
Dr. Guido Solares
Thesis Supervisor
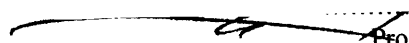
Certified by ....
Prof. Jacquelyn C. Yanch
Thesis Reader

Certified by ....
Dr. Robert Zamenhof
Thesis Reader

Accepted by ....
Prof. Lawrence Lidsky
Chairman, Dept. Committee on Graduate Students

AUG 18 1998 Science

Boron Neutron Capture Therapy
Treatment Planning Improvements
by
John Timothy Goorley

Submitted to the Department of Nuclear Engineering on May 19, 1998,
in Partial Fulfillment of the Requirements for the
Degree of Masters of Science in Nuclear Engineering

Abstract

The Boron Neutron Capture Therapy (BNCT) treatment planning process of the Harvard/MIT team used for their clinical Phase I trials is very time consuming. If BNCT proves to be a successful treatment, this process must be made more efficient. Since the Monte Carlo treatment planning calculations were the most time consuming aspect of the treatment planning process, requiring more than thirty six hours for scoping calculations of three to five beams and final calculations for two beams, it was targeted for improvement. Three approaches were used to reduce the calculation times. A statistical uncertainty analysis was performed on doses rates and showed that a fewer number of particles could not be used and still meet uncertainty requirements in the region of interest. Unused features were removed and assumptions specific to the Harvard/MIT BNCT treatment planning calculations were hard wired into MCNP by Los Alamos personnel, resulting in a thirty percent decrease in runtimes. MCNP was also installed in parallel on the treatment planning computers, allowing a factor of improvement by roughly the number of computers linked together in parallel. After theses enhancements were made, the final executable, MCNPBNCT, was tested by comparing its calculated dose rates against the previously used executable, MCNPNEHD. Since the dose rates in close agreement, MCNPBNCT was adopted. The final runtime improvement to a single beam scoping run by linking the two 200MHz Pentium Pro computers was to reduce the wall clock runtime from 2 hours thirty minutes to fifty nine minutes. It is anticipated that the addition of ten 900 MHz CPUs will further reduce this calculation to three minutes, giving the medical physicist or radiation oncologist the freedom to use an iterative approach to try different radiation beam orientations to optimize treatment.

Additional aspects of the treatment planning process were improved. The previously unrecognized phenomenon of peak dose movement during irradiation and its potential for overdosing the subject was identified. A method of predicting its occurrence was developed to prevent this from occurring. The calculated dose rate was also used to create dose volume histograms and volume averaged doses. These data suggest an alternative method for categorizing the subjects, rather than by peak tissue dose.

Thesis Supervisor: Guido R. Solares
Title: Assistant Professor of Radiology at Harvard Medical School

Thesis Reader: Jacquelyn C. Yanch
Title: Associate Professor of Nuclear Engineering and
Whitaker College of Health Sciences and Technology

Thesis Reader: Robert Zamenhof
Title: Associate Professor of Radiology at Harvard Medical School

Acknowledgments

I would like to thank my thesis advisor, Dr. Guido Solares for his effort and help. I wish him the best in his new pursuits.

I appreciate the helpful thesis review and suggestions given by Dr. Yanch, Dr. Zamenhof, and W.S. Kiger. Thanks for your time and attention.

I greatly appreciate Dr. G. McKinney's personal assistance and supervision of my work at Los Alamos and MIT.

I wish to thank the BNCT group members W.S. Kiger, C. Chuang, K. Riley, M. Ledesma, Dr. R. Zamenhof, Dr. M. Palmer, Dr. P. Busse, Dr. O. Harling, Dr. L.Tang, J. Kaplan, and Dr. I. Kaplan. This group of people has helped make my experience with the BNCT project a personally rewarding academic learning experience.

I would like to thank the Los Alamos National Laboratory personnel that have been extremely helpful. Dr. G. McKinney, Dr. K. Adams and Dr. G. Estes have been supportive during my various stays at Los Alamos and through my other contact with them. I also wish to say thanks to all of the other XTM and XCI personnel that have increased my understanding of MCNP: Dr. J. Hendricks, Dr. J. Briesmeister, and the other instructors I have learned from.

I would like to thank the MIT Reactor personnel for their help with the project. Dr. J. Bernard, T. Newton, and F. Mc Williams have been particularly gracious.

Table of Contents

List of figures

List of tables

1. Introduction

Treatment planning is an integral yet time consuming part of the Harvard/MIT Boron Neutron Capture Therapy (BNCT) Phase I clinical trials. If the clinical trials show efficacy of this experimental treatment, and BNCT becomes a mainstream treatment, the treatment planning must be streamlined. In chapter one of this thesis, the treatment planning procedure is described, providing a written record for the reader. Chapters two, three, and four contain the accomplishments of this thesis work. Chapter two details the methods used to greatly reduce the computational time needed in treatment planning: a voxel dose rate error analysis, modifications to the Monte Carlo computer code, and implementation of parallel computing. Also described are the quality assurance tests used to verify the code.

During this thesis research, a previously unrecognized phenomenon of peak dose movement was identified as having occurred in several of the subject irradiations. Further investigation shows a relation between slight subject overdoses and this phenomenon. This effect was also investigated with relation to the beam geometry of the treatment, either perpendicular or nearly parallel opposed. A method of predicting when this global maximum movement occurs was developed. This phenomenon is described in chapter four.

The retrospective dosimetry calculations for this thesis include dose volume histograms and volume averaged doses. These new volume averaged doses could be used as the basis for reorganizing the subject cohorts, rather than on the peak dose, as required by the existing FDA-approved clinical protocol. Additional calculations produced the difference between peak dose to tissue and peak brain dose. These results are described in chapter five.

2. Harvard/MIT BNCT Treatment

Boron Neutron Capture Therapy (BNCT) was first suggested by Gordon Locher in 1936[1]. Through the application of a boron containing pharmaceutical that is selectively absorbed by a tumor, the tumor receives more dose than the surrounding tissue during subsequent neutron irradiation[2,3,4]. The increase in dose is caused by the short range of the alpha and ^{7}Li reaction products from neutron absorption by a ^{10}B nucleus. This process is currently being investigated by several teams around the globe in the treatment of a variety of cancers[5,6]. The Beth Israel Deaconess Medical Center / MIT group is currently engaged in Phase I clinical trials using the M.I.T. Nuclear Reactor Laboratory's epithermal neutron beam to study the toxicity of neutron irradiation on neural tissue[7,8]. After the phase I study has been completed, it is hoped that a phase II study will show the efficacy of BNCT for controlling Glioblastoma multiforme and metastatic melanoma.

2.1 Treatment Process

The BNCT treatment process includes a variety of steps in addition to the physical irradiation of a subject. Beam characterization, treatment planning, online dosimetry, and retrospective dosimetry are all parts of the BIDMC/MIT procedure. Each one of these topics is described in detail in this chapter. Beam characterization is necessary to ensure the proper dose is delivered during irradiation. Treatment planning optimizes the radiation dose to tissue and tumor. Retrospective dosimetry verifies the proper dose was delivered during the irradiation procedure and is used to correlate effects, such as tumor regression or reoccurrence, or healthy tissue neurological effects, with delivered dose.

The MIT Nuclear Reactor Laboratory's current epithermal neutron beam, m67, is characterized every six months[9]. The fast and thermal neutron and gamma dose rates are measured at various depths of an ellipsoid head phantom. The ^{10}B dose rates are calculated from the thermal neutron flux. The m67 beam is also equipped with two thermal and epithermal neutron detectors, called the beam monitors. The dose rates are proportional to the beam monitor count rates, which are monitored during subject

irradiation. After a calibration is completed, the first stage of the treatment process does not occur until a human subject has been accepted into the protocol.

Treatment planning is the most time consuming aspect of the entire process, taking a minimum of five days to complete even though the actual irradiation takes only a few hours. The treatment planning software, MacNCTPlan, designed and developed at Harvard/MIT, uses CT and MRI data to allow the medical physicist to specify the location of tumor and normal neural tissue, construct a subject specific individual model for radiation transport, and visualize dose rate data from the transport calculations[10,11,12]. During the several days prior to the irradiation, the medical physicist compares the dosimetric result of using different irradiation beam orientations and selects the final beam geometry. Comparisons are based on dose to sensitive locations as well as maximum, minimum, and dose-volume distributions to tumor and normal tissue. These evaluations are based on calculated dose rates from Monte-Carlo simulation of the irradiation. Once the final beam is selected, a more lengthy calculation is performed to reduce the associated statistical error, since the resultant dose rates will be used to determine the length of irradiation.

The Monte Carlo program MCNP*[13] is used to calculate the dose rates throughout the head phantom and the subject for various beam orientations. MCNP is used for a variety of reasons, including its ability to model the subject, represent the epithermal neutron beam's energy and radial distributions and the complex thermalization process of epithermal neutrons[14].

Once the final beam or beams are determined, there is a distinct change in the dosimetry approach, instigated by the written directive of this Phase I protocol. No longer are doses to various locations considered; only the maximum dose to tissue is important, since the subjects are divided into cohorts on this basis. Since the dose contribution from the ^{10}B reaction is roughly one quarter of the total dose to normal tissue, an accurate dosimetry protocol must account for the subject ^{10}B biodistribution during the time of irradiation. Accordingly, the blood ^{10}B concentration is measured with inductively coupled plasma atomic emission spectrometry (ICP-AES) or prompt gamma

10

neutron activation analysis (PGNAA), and the total integral dose to the maximum dose location is determined during irradiation. This calculation relates the beam monitor readings to the dose rates in phantom and the Monte Carlo calculations of phantom and subject dose rates.

After the irradiation is concluded and the final blood boron concentration curve is determined through the least squares fit of the measured data with a double or triple exponential, retrospective dosimetry focuses on the dose to a variety of locations and volume dose, in addition to the maximum dose location. The average dose to neural tissue, the maximum, minimum and average tumor doses are also of interest.

2.1.1 Beam Characterization

The neutron and gamma dose rates of the MIT Nuclear Reactor Laboratory's epithermal beam are measured every six months with an ellipsoid head phantom[15,16,17]. The ^{10}B component is calculated from the thermal neutron fluxes. The phantom is an acrylic shell filled with water. It has several holes in the bottom, which allow the insertion of a radiation detector. Mixed field dosimetry methods are used to determine the magnitude of each dose component. A dual ion chamber is used to measure the fast and gamma dose rates. The cadmium difference method is used to determine the thermal neutron fluxes. The appropriate kerma factors are applied to determine the dose rates from thermal neutrons and the boron capture reaction. All measurements are taken on the central axis of the phantom at one centimeter intervals. The phantom is aligned with the beam's axis and its apex is located one cm below the ceiling of the medical room. The beam counters measure the neutron flux associated with each set of axial dose rate measurements. The neutron flux varies proportionately with reactor power, which is typically 4.8 MW during the phantom measurements and subject irradiation. The immediate result of this measurement is the correlation of beam count rates with phantom dose rates.

---

* MCNP is a trademark of the Regents of the University of California, Los Alamos National Laboratory

The axial dose rates in phantom are independently calculated by MCNP. Although the dose rates to every 1 cm³ voxel within the 21 cm by 21 cm by 25 cm model of the head phantom can be calculated, only the dose rates along the central axis are compared to the experimental data. In a process similar to the modeling of the subject, which is described later in this chapter, the phantom is modeled in MCNP as a water ellipsoid with the air holes in the bottom where the detectors are inserted. Neutron and photon dose rates are calculated for each cell. The boron dose is determined from the thermal neutron flux in each cell.

Measured and MCNP calculated dose rates are then plotted as dose rate vs. depth, as shown in Fig 2.1a-e. The fast neutron, thermal neutron and boron dose rates are directly compared. MCNP calculates the dose rates from the structural gammas and induced, or capture gammas, individually, which are compared to the measured gamma dose rate, or the sum of the two.

Figs. 2.1a-d show the adjusted MCNP phantom dose rates and experimental data for the June 1997 characterization[18].
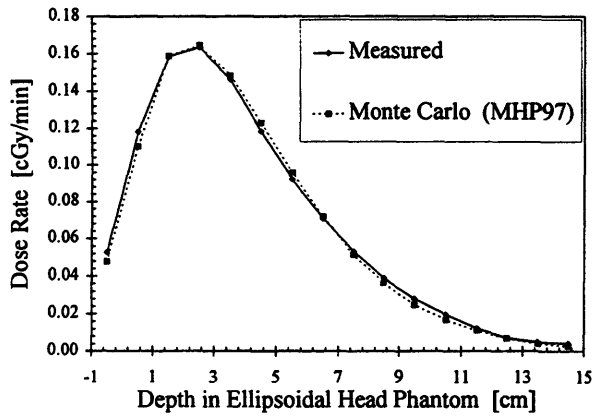
Figure 2.1a. Thermal Neutron Dose Profile   Figure 2.1b. Fast Neutron Dose Profile
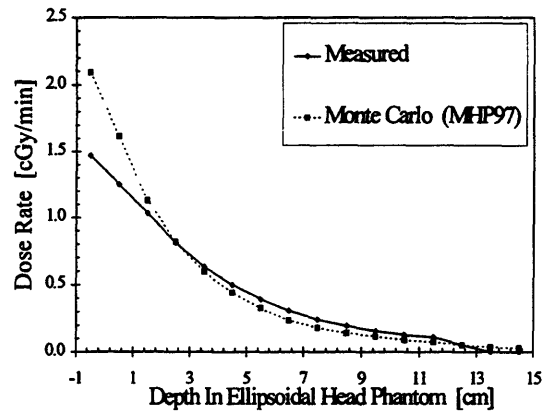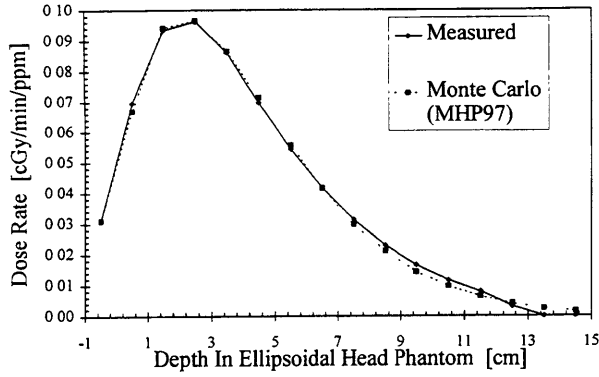
Figure 2.1c. ^{10}B Depth Dose Profile
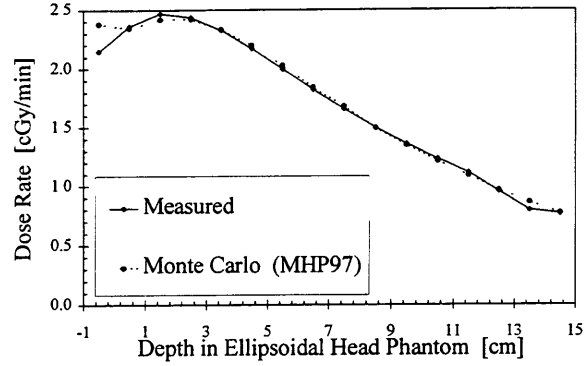
Figure 2.1d. Photon Depth Dose Profile

Using the dose rate vs. depth data, the least squares difference scaling factor is then found. For the gamma component, a scaling factor for each MCNP dose rate is used. These scaling factors physically account for the difference between experimental dose rates and the calculated MCNP dose rates. With this correction factor, the doses from MCNP can then be considered as the physical dose rates occurring in the subject. Typical scaling factors, shown in Table 2.1, are near unity, indicating that there is a strong agreement between dose rate calculations and measurements.

Table 2.1 Scaling Factors for the June 1997 Characterization

Thermal N	Fast N	^{10}B	Induced γ	Structural γ
0.824	1.088	0.805	0.901	1.810

2.1.2 Treatment Planning

Individualized subject treatment planning begins when a subject enters the protocol. The major steps include MCNP simulation of the irradiation, relation of subject and phantom MCNP dose rate results and calculation of anticipated irradiation time.

The introduction of individualized subject data begins with CT scans and MRIs. These images allow the physician to localize potential tumors, as well as construct a model using subject specific data. As with the phantom data, the images are imported and processed as follows. Within MacNCTPlan, the images are thresholded to

differentiate air, soft tissue and bone, which are included in the model. Several potential beam orientations are designated. MacNCTPlan also voxelizes the subject data into 1 cm^3 cells. These data are converted into a MCNP input deck, and MCNP is run to determine the dose rates in each voxel for each beam orientation. Each potential beam is run so that its statistical error is on the order of five percent in the region of interest. One or two final beams are chosen and they are run until the statistical error is around one percent in the region of interest.

The dose rate scaling factors, created by the phantom calibration, are also applied to the subject Monte Carlo data to obtain the representative physical dose rates throughout the subject. The maximum physical dose rates in the phantom and subject are then determined for anticipated boron concentrations, typically 15 and 12 ppm for the first and second beams. The ratio of the maximum of the two dose rates is called the Monte-Carlo Dose Rate Ratio (MCDRR). When the peak dose rate measured in phantom during the axial irradiation is divided by the MCDRR, the result is the physically occurring peak dose rate in the subject from a specific, non axial, radiation beam orientation. Although the MCDRR relates physical dose rates, it is based on the calculated dose rates and the scaling factors, and hence will vary with the curve fit used. Since the MCDRR is a ratio of the dose rates, small fluctuations in scaling factors will have no significant impact on the MCDRR value.

After the final dose rates have been determined, the length of irradiation is estimated. For one beam irradiations, the prescription dose is divided by the maximum dose rate occurring in the subject, or the MCDRR times the maximum phantom dose rate. For a dual beam irradiation, the process is more complex. Using MacNCTPlan, the dose rates from both beams are added, assuming some neutron fluence weighting factor between the first and second beam, as described in section 2.2.5. Once the dose rate distributions of both the beams are added, the maximum dose rate location is calculated. The ratio between a beam's maximum dose rate to the combined global maximum dose rate is calculated. Using this ratio, which accounts for the beam weighting, and the prescription combined global maximum dose, the target dose from each beam is calculated for that beam's peak dose. During the irradiation the beam's peak dose is

14

determined by the count rates and boron biodistribution as described in the following section.

2.1.3 Irradiation Procedure

The current protocol used by the BNCT group defines the intended target dose, the prescription dose, as the maximum dose occurring within any non-tumor tissue. The maximum dose location will vary with number and orientation of beams, and can occur in scalp, skull or brain. This prescription dose is incrementally increased by ten percent with each new cohort. The previous dose steps have been 880, 990, 1065 RBE cGy.

At various times throughout the infusion and irradiation, 1 ml blood samples are taken to determine the boron concentration. These samples are analyzed with either inductively coupled plasma atomic emission spectrometry or prompt gamma neutron activation analysis[19,20]. The resulting biodistribution curve is fit with a double or triple exponential.

To ensure the best calculation of subject dose, the cumulative dose is recalculated as the subject's biodistribution curve is measured. There are two methods currently used by the group. The method developed by Dr. Guido Solares allows almost instantaneous dose calculations and evaluations[21,22]. His computer is taking continuous readings from the beam counters. The second method developed by the group is slightly more discrete. The "laptop" calculations recalculate the cumulative dose to the subject every fifteen minutes, and more frequently near the end of irradiation. These calculations account for the subject's boron biodistribution curve and the effective power of the reactor.

The beam monitors measure the neutron rates and are a direct reflection of reactor power. Reactor power will vary throughout the irradiation, during startup, shutdown and subject repositioning. This variation affects dose rates and the delivered dose during the irradiation. By dividing the beam monitor measurements during subject irradiation by measurements during the phantom irradiation, the effective reactor power is found over a given time interval. When this ratio is divided by the MCDRR, multiplied by the measured phantom dose rates and a particular time interval, the peak dose delivered by

the non-boron components to the subject is calculated. The associated boron dose is multiplied by the average boron concentration during the time interval.

The effective reactor power is used to calculate the effective full power irradiation times and the effective boron concentration for each beam after the irradiation is concluded. These two post irradiation quantities will be used to calculate the retrospective doses from the Monte Carlo dose rates.

2.1.4 Laptop Retrospective Dosimetry[23]

The effective irradiation time for each beam is a measure of full power irradiation time, and is multiplied by the calculated dose rates, scaling factors, and boron concentration to find the delivered dose to any location within the subject model. Equation 2.1 shows that for a dual beam irradiation, the delivered dose to the ith voxel is the sum over the two applied beams, B1 and B2, of the dose rates multiplied by their respective effective irradiation times.

$$\text{Dose(i)} = \text{DR(i)}_{B1} \cdot T_{B1} + \text{DR(i)}_{B2} \cdot T_{B2} \qquad \text{Equation 2.1}$$

The dose rate, DR(i), in equation one includes the boron dose rate component, which should be multiplied by the beam's effective boron concentration. The effective boron concentration for the first beam, $B_{B1}{}^{Eff}$, is the power weighted time averaged ^{10}B concentration during a given beam. It is calculated using equation 2.2, where a and b are the beginning and end of the irradiation beam, B(t) is the boron concentration as defined by the final boron biodistribution curve, which includes ^{10}B concentration measurements several hours after the irradiation has concluded. $P^{Eff}(t)$ is the effective power. The other beams are calculated in the same way.

$$B_{B1}^{Eff} \text{ (ppm)} = \frac{\int_a^b B_{B1}(t) \cdot P_{B1}^{Eff}(t) \cdot dt}{\int_a^b P_{B1}^{Eff}(t) \cdot dt} \qquad \text{Equation 2.2}$$

16

The biodistribution curve, along with the two physical parameters of actual irradiation times and reactor power, are fixed and will not change with dose recalculations, nor will the effective boron concentrations and irradiation times. The post -irradiation values are used by MacNCTPlan in calculating a new MCDRR, which is then used to recalculate the peak dose delivered to the subject in the laptop dosimetry spreadsheet. Since the dose is based on measured values, the retrospective laptop dose is the best estimate of the peak dose delivered.

2.1.5 MCNP Retrospective Dosimetry

Although the phantom measurement based dosimetry provides an accurate peak dose in the phantom, it fails to determine the subject's final dose distribution, which has important clinical significance. While the calculated dose rates are the only current method of determining off axis dose rates, they do rely on the least squares fit of the scaling factors. In cases where the measured and calculated values differ, it is possible to use the calculated dose distributions and infer that the supposed peak dose was significantly higher than was actually delivered. Figure 2.1b shows the calculated fast neutron dose rate at 1 cm is fifteen percent higher than the measured dose rate. However, since the least squares fit is applied over the entire curve, the volumetric dosimetry is a reasonable approximation.

In the retrospective analysis, the doses to tumor and tissue are determined in addition to the maximum dose. Within MacNCTPlan, the neural tissue can be identified and marked in the same manner as the tumor. The volume of neural tissue for each voxel can be determined, as can the total volume of neural tissue in the head. The volumes calculated have been slightly higher than the anticipated values based on ICRP, but tend to agree well with a newly constructed phantom model adopted by the MIRD comittee[24,25]. Once the volumes of tumor and tissue have been calculated, their corresponding dose distributions can be used for volumetric dosimetry.

The retrospective doses to various locations are determined differently. The peak or prescription dose is best determined with the laptop dosimetry, while average doses

17

can only be determined with MCNP. Calculation of the volume averaged doses requires knowledge of the three dimensional dose distributions, which is only gained from the MCNP calculations. Currently the depth vs. dose rate distribution along the beam's axis only is obtained from phantom measurements.

Using the dose to each voxel and the fraction of each voxel that is either tumor or tissue, it is possible to calculate the volume of tissue or tumor that receives a certain amount of dose or higher. This plot is referred to as a dose volume histogram, or DVH.

DVHs are used by radiologists to visually determine the advantage dose, or the additional dose the tumor receives to that of normal tissue. Dose volume histograms, in low dose ranges, show the effects of beam geometry, with subjects with parallel opposed beams having significantly higher volume doses than subjects with single or orthogonal beams. In high dose regions, the x intercept, or peak dose, is a function of the prescription dose.

2.2 Treatment Planning Process

The objective of treatment planning is to provide a timely method for determining the best overall RBE dose distribution to healthy tissue and tumor. For healthy tissue, the maximum dose rate and dose rates to sensitive structures are considered. For the tumor, increased ^{10}B concentrations and RBE's may be accounted for in calculating the minimum dose rate. Both the tumor and normal tissue dose distributions will vary with the orientation of the neutron beam or beams. The treatment planning software, MacNCTPlan developed at Harvard and MIT, allows these dose rate distributions from single beams or combinations of beams to be compared. To achieve this end result, several tasks must be completed. In part one of MacNCTPlan, CT and MRI images of the subject are used, after processing and registration, to localize the tumor and generate a model of the subject. MCNP calculates dose rates throughout this model. In part two of MacNCTPlan, the dose rates are then visualized as isodose contours superimposed over the CT or MRI images. This allows the medical physicist to evaluate different beam orientations.

2.2.1. Preparation

The acquisition of subject CT and MRI scans is the first part of the treatment planning process. In a single image series, about one hundred thirty images of parallel planes two millimeter apart are collected. Image acquisition is done such that planes start in the air located above the head and finish near the superior portion of the shoulders. Each pixel in a CT image is represented by sixteen bits, but the image contains only 12 bits of information. The twelve bit Hounsfield numbers indicate the attenuation coefficients in the individual. The Hounsfield number is simply an integer ranging from -1024 to 4096. A single CT image file is a listing of each pixels' Hounsfield number in addition to a file header. Each CT image is 512 pixels wide by 512 pixels tall. The MRI images are also sixteen bit images, but are 256 by 256 pixels. These files are obtained with proprietary medical systems, such as the GE or Siemens scanners at the BIDMC, but are transferred to the Harvard/MIT BNCT Macintosh computers using the DICOM protocol.

For both imaging modalities, at least two series are obtained: one with contrast (+) and one without (-). The contrast agents, containing Iodine (I) and Gadolinium (Gd), are used for CT and MRI, respectively. These contrast agents cause the subject's edema and tumor to be more visible in the computer images. While the four image sequences, I+, I-, Gd+ and Gd-, are available, not all of them are used, particularly if the tumor and edema are visible with CTs.

Before they can be used in MacNCTPlan, the CT and MRI images must first be processed. The files are first transferred to a Macintosh computer, using the DICOM protocol. All the files are then imported using the public domain program, NIH Image. NIH Image reads the actual data, but not the header. By subtracting the number of bytes the data occupy from the file size, the header size can be determined. The CT data occupy 16 bits times the image size, 512 by 512 for a total of 524,288 bytes. Using file menu command import, the header size is entered and the file is imported as raw data.

This importing process automatically coverts the 16 bit images to 8 bit, with a spectrum of 256 pixel intensities. This mapping can compress all available 12 bit intensities, into 8 bit intensities, or a specific range of intensities, for example 1000 to 2048, can be mapped onto the intensity range, as illustrated in figure 2.2.

16 bit ⟶ 8 Bit   16 bit ⟶ 8 Bit
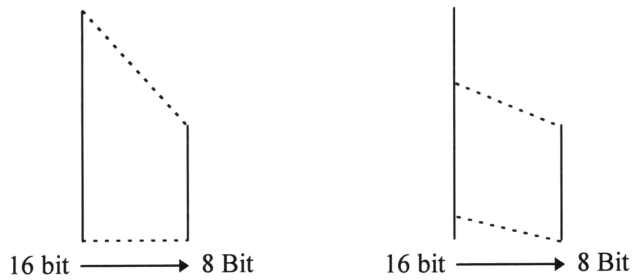
Figure 2.2 Mapping 16 bit images into 8 bit images.

The image mapping on the left will produce an 8 bit image that contains the entire 16 bit domain. The image mapping on the right will produce an 8 bit image that contains only a specified domain of pixel intensities.

Figure 2.3 shows the same CT image with and without this subrange specified.
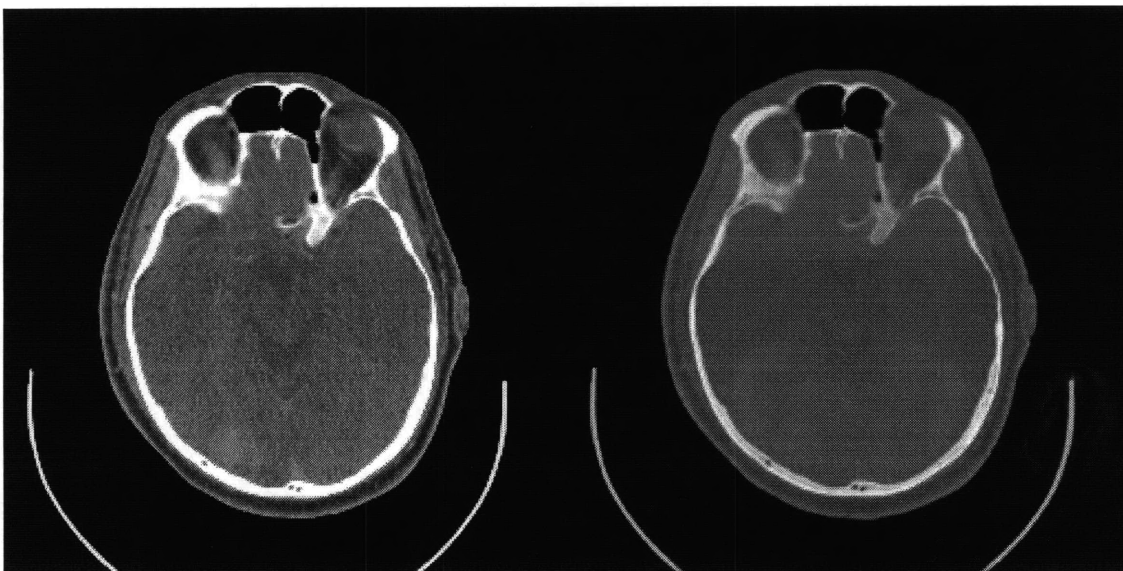
Figure 2.3 I+ Imported Images. The image on the left represents a subrange of all pixel intensities, while the image on the right is a complete mapping of all intensities. These images are 256 bit by 256 bit.

20

It can be seen that this subrange specification is thresholding the image. Since several of the unwanted artifacts, such as those produced by towels, have very low intensities, this thresholding reduces the amount of image processing and "cleaning" that must be done.

The final conversion step is to reduce the CT stack to 256 by 256. This size reduction is completed with the NIH Image scale command, where both the x and y directions are scaled by 0.5. The image intensities are then inverted, or subtracted from 256. The resulting stack is then saved in the TIF file format.

Once all image files have been imported and converted into a single stack, the artifacts are removed. The head holder, towels, and other external objects are removed in each slice. The eraser tool can be used to remove them manually, or the magic wand thresholding tool can select a contiguous body in each slice, such as the cross section of the head, which is then copied on to a new 256 by 256 window. If the subject has metal fillings, there will be several planes that contain shadows. These planes are replaced by the nearest usable plane. Although this will cause the model to be unrepresentative of the subject, this approximation is made in a region far from the beam entrance location and will negligibly affect the dose to the region of the tumor and upper skull. After being cleaned, the stack is saved as a TIF file. Figure 2.4 shows two images, the first showing the shadows associated with metal fillings, the second showing the best replacement image. These images also show the head holder and towels clearly.
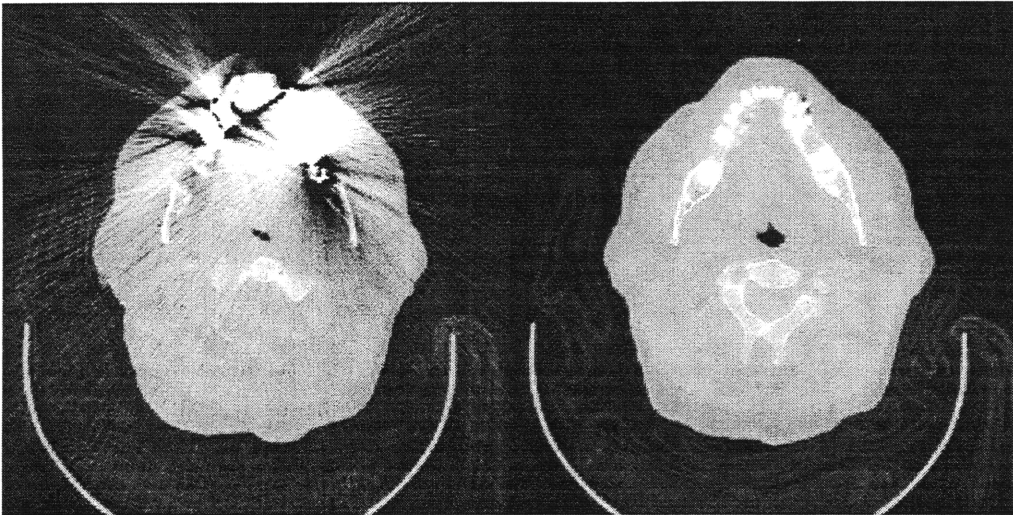
Figure 2.4 Metal Filling Artifacts and Replacement.

Occasionally, the tumor is plainly visible from the I+ stack. Since the I+ and I-stacks are typically acquired with the subject in the same position, the images are already aligned. Since the tumor is visible in the aligned I+ stack, the time consuming registration of the MRI and CT stacks becomes less necessary for treatment planning. More often, however, the tumor is only clearly visible from the Gd+ images. Since the subject model construction uses the I- images to avoid thresholding problems described later, the Gd+ stack must be aligned with the I- stack. Each plane in the Gd+ MRI stack is made to correspond to the I- CT plane with the same physical characteristics. For example, the fourth plane in the CT stack, corresponding to a plane eight millimeters from the top of the head, perpendicular to the central axis, is the fourth plane in the MRI stack and exhibits the same physical features. Unfortunately, since the head is typically in different orientations during scans, the Gd+ stack must be translated, scaled, and rotated, often in two dimensions. Image registration is not a trivial task and is the subject of ongoing research. To aid the process, the subject wears a latex swim cap with several fiducial markers, in this case Vitamin E tablets, that are easily visible in both imaging modalities. Fig 2.5 show I-, I+ images and their corresponding Gd+ image with fiducial markers.
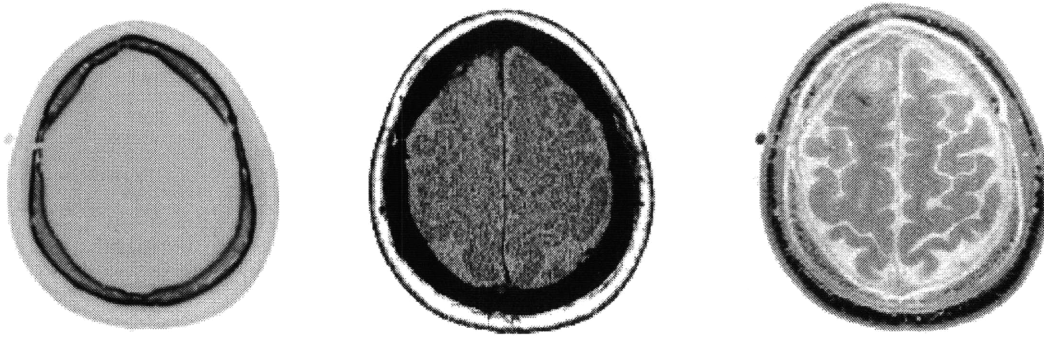
Figure 2.5 I-, I+, Gd+ Images of the same plane with fiducial markers. The tumor is in the upper left of each image. The images have been mapped with different ranges.

2.2.2 MacNCTPlan Part I

In the first phase of MacNCTPlan, preparations for transport calculations are made. The subject's CT and MRI scans are used to determine the tumor's location. Based on the tumor's location and the medical physicist's experience with previous dose distributions, three to five potential 3-D beam orientations are determined. The CT images are used to construct a model of the target region, i.e. the subject's head, or other body part. Discrimination between bone, air and soft tissue is determined from the Hounsfield numbers of the CT image. The stack of CT images is divided into a lattice of 11,025 one cm^3 cells. The fraction of air, tissue, tumor and bone, is determined to the nearest twenty percent in each cell. This information, in addition to estimated boron concentrations in tissue and tumor, is then used in constructing an MCNP input deck. While there are additional steps within MacNCTPlan Part 1, only the ones significant to model construction will be described.[1]

After the Gd+ files have been opened in MacNCTPlan, the tumor localization (outlining) is directed by the physician. For each slice, the tumor is defined (outlined) by drawing a line around it. This line defines a region of interest, or ROI. When all of the tumor has been outlined, the ROI is saved in a separate file to be used with the I- stack. When this step is completed, the I- stack is opened and used for the remaining

MacNCTPlan Part I procedures. The screen shot of MacNCTPlan in figure 2.6 shows the tumor localization.

Outline Tumor   Part - I

1	2	3	4	5	6	7	8	9	10	11	12	13	14	15	16	17	18	19	20	21	22	23	24	25	26	27	28	29	30
31	32	33	34	35	36	37	38	39	40	41	42	43	44	45	46	47	48	49	50	51	52	53	54	55	56	57	58	59	60
61	62	63	64	65	66	67	68	69	70	71	72	73	74	75	76	77	78	79	80	81	82	83	84	85	86	87	88	89	90
91	92	93	94	95	96	97	98	99	100	101	102	103	104	105	106	107	108	109	110	111	112	113	114	115	116	117	118	119	120

| 121 | 122 | 123 | 124 | 125 |

L   W

[Original]

Exit   Save   ◀ ■ ▶   Image   34   ROI   Mark   Redo   34   Ref. ROI

Figure 2.6 Screen Shot of MacNCTPlan Tumor Outlining

The next step within MacNCTPlan is to differentiate air, bone and soft tissue by thresholding the pixel intensities. Since the images were inverted, the air is colored white due to its low image intensities, while the bone is dark at high image intensities. MacNCTPlan allows the user to adjust the pixel intensity threshold for any slice and color the corresponding air, tissue or bone blue, green or red respectively. The coloration allows visual feedback as the threshold is changed. Figures 2.7 is a MacNCTPlan screen shot showing the thresholding step in MacNCTPlan. The reason that the I- stack is used now becomes obvious. The I+ stack, if thresholded, would contain bone in locations that it does not exist. The MRI stack does not lend itself to thresholding, since the bone and

air are similar in intensity. Even if the image is inverted and the air is artificially colored white, the thresholding problem is even worse than in the I+ stack.
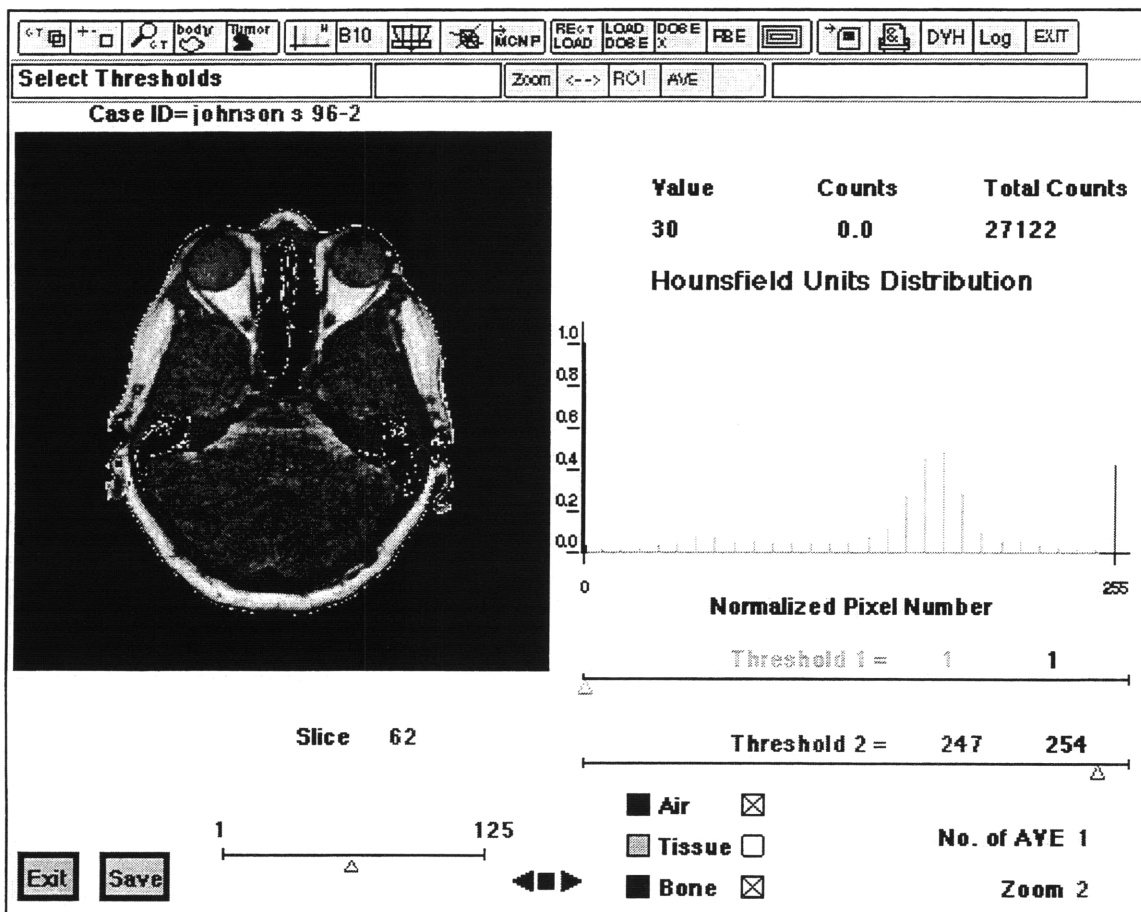
Figure 2.7 Screen Capture of MacNCTPlan Thresholding

The next significant step after thresholding is the determination of irradiation beam orientations. The medical physicist uses his experience of dose distributions to determine three to five possible beams. Deep tumors usually receive a bilateral irradiation to increase dose to regions that would have low dose contributions from the first beam. To precisely define the exact entrance and exit locations of the beams, the stack is manipulated in three dimensions, allowing two cross hairs to be placed at the preferred entrance location. To guide the medical physicist, the irradiation beam's central axis and edges are displayed superimposed over the reconstructed CT images of two

25

orthogonal planes along the central beam axis. Figure 2.8 shows a screen capture of the beam direction portion of MacNCTPlan.

X =   -67.30
Y =   73.64
Z =   -16.00
[mm]

Plot Panel
—> Left

Plot   Print   Save   Reset   Laser

Tilt Angle =   0   Degree
Rotation =   245   Degree
Horizontal Offset =   94.2   mm
TransAxial Offset = 110.0   mm
Vertical Offset =   40.4   mm

Beam   1

	X	Y	Z
Entrance (mm)	56.72	84.55	-16.00
Exit (mm)	-81.63	-27.48	-16.00
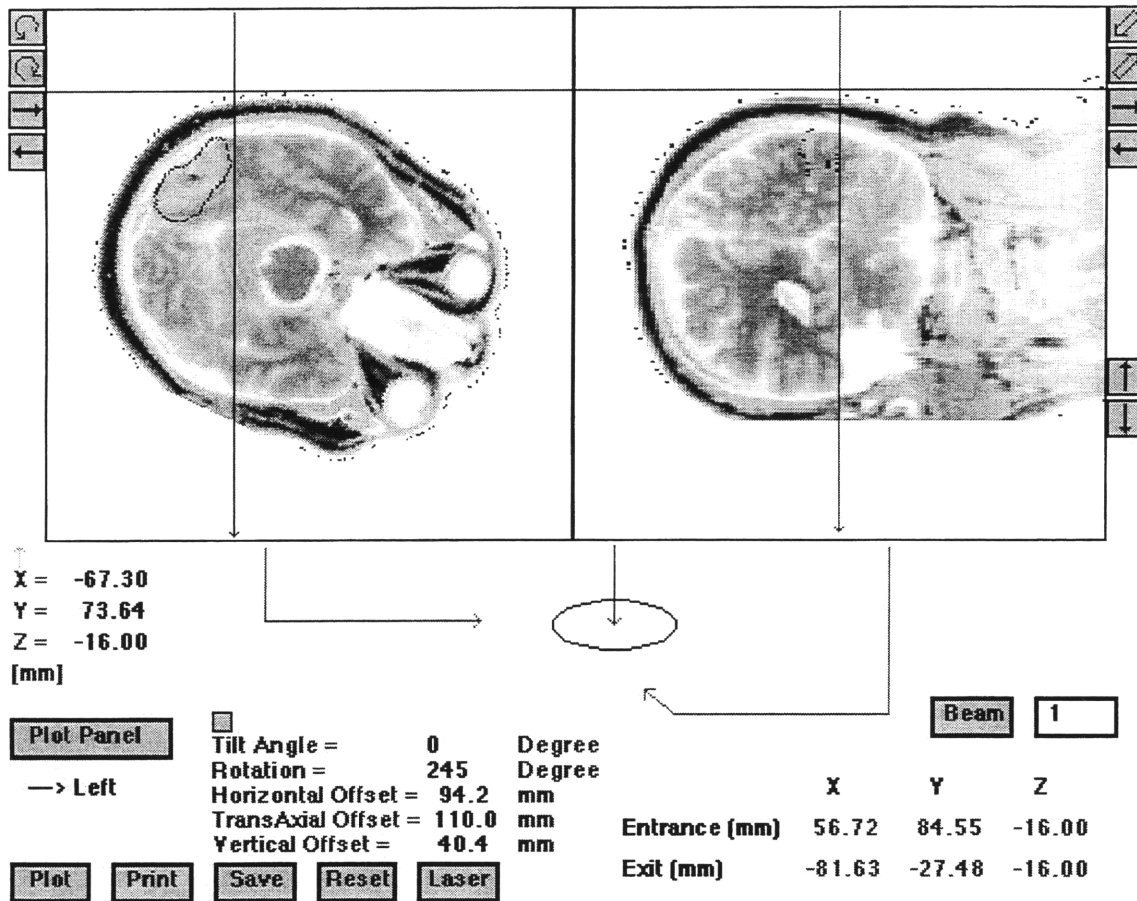
Figure 2.8 MacNCTPlan Screen Capture of Beam Positioning

The final important step is the creation of the head model, a 21 cm by 21 cm by 25 cm lattice of 1 cm^3 cells. The CT data in each cell are represented as a certain percentage of soft tissue, tumor, bone and air, rounded to the nearest twenty percent. This averaging process uses nearby pixels in the same plane, as well as adjacent planes. After voxelization, each cell's location and composition is saved to a materials file. This file also includes the beam entrance and exit locations, thresholding values and anticipated boron concentrations for each beam set in previous portions of MacNCTPlan. Figure 2.9 shows a CT slice and its corresponding voxelized data.
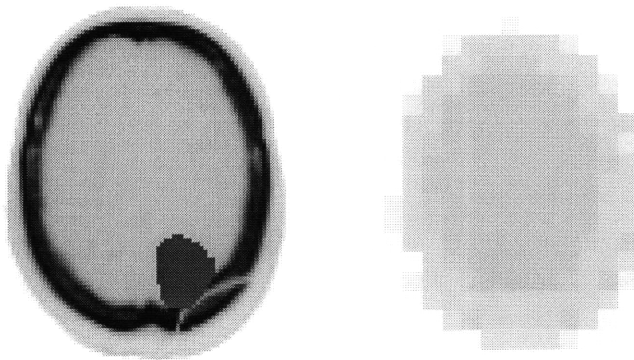
Figure 2.9 MacNCTPlan CT Voxelization

2.2.3. MPREP

More information is needed to create an MCNP input deck. The FORTRAN 77 program MPREP incorporates the MacNCTPlan materials file with files containing other information necessary for MCNP. The spatial, angular and energy characteristics of the neutron and photon beams, as well as the kerma factors for each dose component are required. MPREP also prepares this information in the format required for the MCNP input deck, calculating the necessary surfaces, planes, and material fractions.

The MCNP materials themselves are each a different combination of air, bone, tumor and soft tissue. For example, MCNP material 11 is 20 % bone, 80% normal tissue, while MCNP material 32 is 20 % tumor, 40 % bone, 20 % normal tissue and 20% air. This material may appear in a cell containing the scalp and some surrounding air, the cranium and a portion of a tumor near the surface. There are fifty six combinations of materials, although not all of them are used in a given model.

MPREP converts the cells into the appropriate lattice model. It can also represent the cells individually, without the lattice structure. Since MCNP cannot have photon and neutron sources in the same input deck, MPREP creates photon and neutron input decks for each beam. Figure 2.10 shows the head model of the non lattice version. The visualization program Sabrina cannot display lattices, although the picture would be

similar. The two versions, lattice and non lattice, have different memory requirements and run times, as described in sections 2.3.1 and 2.3.2.
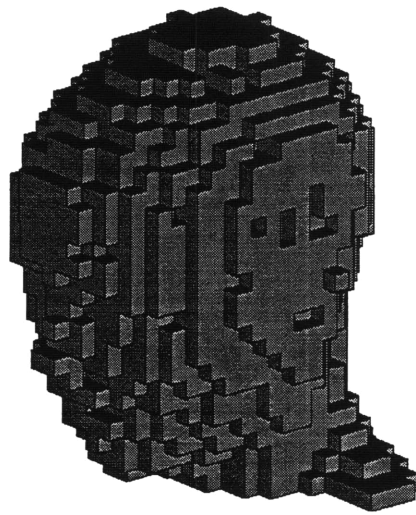
Figure 2.10 Sabrina 3-D representation of the head model. The head is pointing to the left.

2.2.4. MCNP Calculations

After the neutron and photon input decks are created for each beam, MCNP uses them to calculate the dose rates for each voxel. A more detailed explanation of the input decks is given in chapter 3. Typically, one to three million particle histories are used to for scoping runs, which generate results with 5% statistical error in the region of interest. A description of this error and the number of particles used in scoping runs is given in section 3.1.1.

2.2.5. MacNCTPlan Part II

After MCNP calculates the dose rates, the second part of MacNCTPlan is entered. The voxel dose rates for each beam are loaded into MacNCTPlan. From this information, MacNCTPlan interpolates the dose rate to each pixel using a 3D cubic spline. The dose rate data are then shown as isodose contours superimposed over the brain morphology. Tumor and normal tissue isodose rate contours are separately displayed superimposed over the entire brain. The medical physicist then compares the therapeutic ratio of the

minimum tumor dose rate to the maximum normal tissue dose rate, assuming some average boron concentration for each.

The maximum and minimum ratio of tumor dose rate to maximum normal tissue dose rate is then determined for various beam orientations. Using MacNCTPlan, various slices of the tumor are viewed and the appropriate dose rate is recorded. MacNCTPlan can calculate this ratio when the user specifies the normalization factor to be the healthy tissue maximum dose rate, so isoratio contours are plotted. Both visualization techniques allow the medical physicist to obtain an understanding of the volumes encircled by a particular threshold. With the current MIT epithermal neutron beam, the maximum therapeutic ratio is on the order of three or four. The minimum depends heavily on tumor location, and can be less than one for deep tumors.

In cases where the tumor is located near the eyes or optic chiasm, the dose rate to these radiation sensitive structures is determined. If a dual beam irradiation is being considered, the dose distributions from both beams are assessed. To calculate the dose to a sensitive structure, it is assumed that the maximum dose rate location will receive the prescription dose. The prescription dose can then be divided by the ratio of the dose rates to the sensitive structure and the maximum tissue location to determine the absolute dose to these locations. If the dose is unacceptably high, another beam orientation or weighting is selected. The dose to parotid glands, a sensitive structure as reported by Brookhaven National Laboratory (BNL), is also occasionally evaluated if they are in high dose rate locations. To lower the dose to these structures, a posterior beam entry was used.

Although MacNCTPlan gives the medical physicist absolute control over where to place the beams, the actual physical setup used will be limited by the range of the subject positioning device (couch) and the subject's tolerance of discomfort and his or her flexibility. Typical limitations are around twelve degrees lateral tilt of the positioning device, combined with the subject's physical ability to turn his or her neck. For example, irradiation beams cannot be directed into the center of the back of the head in a transverse

plane because the subject cannot be placed face down, nor would it be optimal for the beam to pass throughout the positioning device's headrest.

Occasionally, the medical physicist determines that a small dose to the deep portions of a tumor from a beam entering the contralateral side of the subject's head will yield the best therapeutic ratio. This effect can be accounted for by adjusting a fluence weighting factor. It is the ratio of neutron fluence in the second beam to that of the first. Since the neutron fluence rates may vary slightly, this ratio is not strictly the ratio of the length of irradiations, but is often considered as such.

The physician will occasionally be interested in the use of dose volume histograms (DVH). These can be generated within MacNCTPlan or calculated in an Excel spreadsheet directly from the MCNP data (see section 5.1). In MacNCTPlan Part II, the tumor ROIs can be used as a guide to determine the volume of interest, or the brain tissue or a sensitive structure volume can be outlined and defined as the new ROI. MacNCTPlan will automatically calculate the volume identified, and the relative volume containing a certain dose rate or higher. Below is a screen shot of MacNCTPlan's dose rate volume histogram (DRVH) generation ability. Since the effects of different ^{10}B concentrations and irradiation times can be included, these DRVHs will show an identical shape as the DVH.

After the final beam selection has been made, each final beam calculation is run for ten million source particles, which results in one or two percent error of total dose to the tumor region. This calculation typically requires a run time of fourteen hours on a 200 MHz Pentium Pro computer.

2.3 Monte Carlo N Particle Radiation Transport Code (MCNP)

Determining dose rates to locations in the subject is an integral part of BNCT treatment planning. The Monte Carlo radiation transport code, MCNP, is the integral part of calculating the dose rates. MCNP, a well tested and documented code developed by Los Alamos National Laboratory (LANL), is successful at simulating the complexities of the irradiation. As mentioned before, it is capable of representing the subject's head, the

energy, angular, and radial distributions of the neutrons and gammas emitted from the MITR-II Medical room's epithermal neutron beam. Since the beam contains thermal, epithermal and fast neutron components, MCNP's detailed transport calculations are used to calculate the thermalization and subsequent dose of neutrons through elastic and inelastic collisions with varying isotopes, in addition to the photons created by neutron absorption. When elevated concentrations of ^{10}B are present in the model, MCNP calculates the amount of flux depression and the corresponding change in the dose distribution. MCNP does not track the radiations from the delayed decay of radioisotopes, nor does MCNP include photoneutron creation.

MCNP uses an input file, or input deck, that completely describes the model of the problem that the user wants to simulate. Everything from source characteristics to output format is controlled through this input deck. Significant components of a deck used for BNCT treatment planing are the geometric patient model, either lattice or non lattice based, materials entries, source description, kerma factors and tallies. Each of these is described in detail in this chapter. For a more complete description of input deck options, the reader should refer to the MCNP 4B Manual[12].

2.3.1 Lattice Model

The lattice model of MCNP is a geometric structure: a grid of regular hexahedra, either cubes or triangular prisms. The grid is formed by an infinitely repeating array of regularly spaced planes. A contiguous region of space bounded by these planes is a single lattice element. Since each lattice element can contain several objects, including other nested lattices, a system of layers, or universes, is used to fully describe the model. A universe is a region of infinite space.

The universe structure for the BNCT patient modeling involves three levels, as illustrated in two dimensions in Fig 2.11.
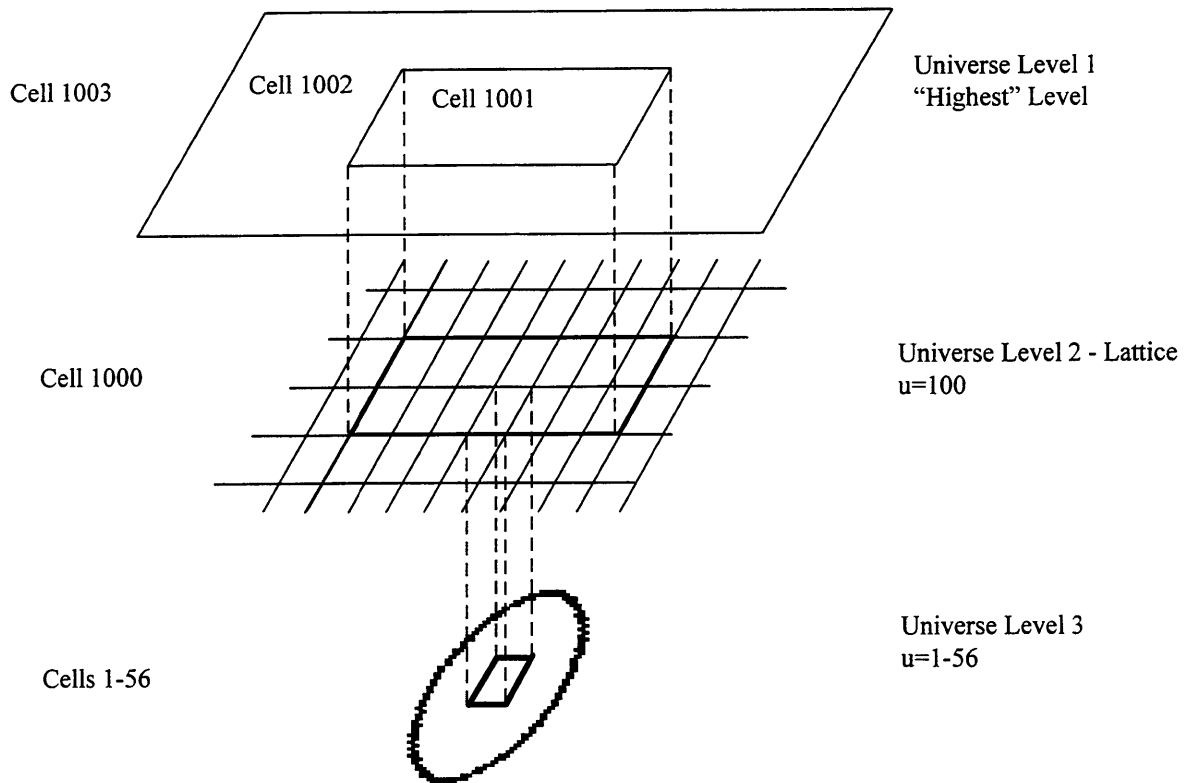
Figure 2.11 Illustration of Multiple Universe Levels. Although only one cell in universe level three is shown, each lattice element has a corresponding cell.

The root universe, or "highest" level, contains the "window" (cell 1001) looking onto the lattice level. Since the lattice is an infinitely repeating structure, it is this "window" which defines how much of the lattice will be visible in the root level, or used for transport. The window is filled with universe 100, which is a cubic lattice (cell 1000). Each lattice element is filled with a lower level universe. This third and lowest level contains cells (cells 1-56) with specified material properties. Just as in the lattice cell, only the portion of these cells that corresponds to the movement of the particle through the lattice element will actually be used. The other two cells in the root level, cell 1002

and 1003, define everywhere external to this window. Cell 1002 is the region of air surrounding the 21 cm by 21 cm by 25 cm model where neutron and photon transport is important. Cell 1003 is a sphere beyond which no transport occurs. Particles passing into cell 1003 are terminated.

The portion of the Harvard/MIT BNCT treatment planning input deck describing the above model is shown in figure 2.12.

```
c       cell cards
c
 1000    0    -112    111  -212    211  -312    311
         lat=1 fill=    0:  20     0:  20     0:  24
         56 56 56 56 56 56 56 56 56 56 26 26 26 26  1 26 56 56 56 56 56 56
[many more lines of data]
         56 56 56 56 56 56 56 56 56 56 56 56 56 56 56 56 56 56 56 56 56 56
         u=100
    1       1  -1.04700E+00      -70 u=    1
[all other universe material cards]
 56      56  -1.29300E-03      -70  u=    56
 1001    0 111 -113 211 -213 311 -313 fill=100      $ Window
 1002    0  -1000 ( -111: 113: -211: 213: -311: 313) $ Outside Window
 1003    0    1000                                   $ No Transport Beyond
Here
c       BLANK LINE

c       BLANK LINE
c
c       surface cards
  111   px    -10.500000                $ Set of Planes in X direction
  112   px     -9.500000
  113   px     10.500000
  211   py    -10.500000                $ Set of Planes in X direction
  212   py     -9.500000
  213   py     10.500000
  311   pz    -10.500000                $ Set of Planes in X direction
  312   pz     -9.500000
  313   pz     10.500000
 1000   so  5.56417E+01
   70   so  5.56417E+01
c
```

Figure 2.12 MCNP Lattice cells and surfaces.

In this example, cell 1000, the lattice, has material zero (i.e. void), and is bounded by the planes 112, 111, etc. These planes form a single 1 cm^3 voxel. Although this voxel is repeated infinitely in the three Cartesian directions, the window bounded by planes 111, 113, etc., limits transport in that universe level. The location of this voxel is such

33

that the center voxel of the entire 21 cm by 21 cm by 25 cm matrix of voxels is at the coordinate (0, 0, 0). The order of the listed planes is important in defining the indices and in what direction they increase. Since 112 is listed first, the voxel in the same y, z location but at -9.0 would be [1,0,0]. The lat=1 option specifies that the lattice is filled with hexahedra, while lat=2 would fill the lattice with hexagonal prisms. The fill option specifies the number of the universe in the next lower level. The listing of fifty-six different universes for each of the 11025 lattice elements specifies which universe each lattice element is filled by. After the lattice cell entry is a listing of fifty-six cells, each specifying a density and material, 1 through 56, belonging to their corresponding universe listed on the lattice card. These cells, although they could be cubes or any other shape that defines the bounding surfaces of a cell, are spheres for simplicity.

After the cell listings is a blank line followed by the surface listings. These surface cards describe planes and spheres that bound the lattice and the regions of importance. This input file uses the new ability of MCNP4B to have coincident window and lattice bounding planes, previously a small offset was required Although not shown above, the imp card sets the importance of every cell to 1, except cell 1003, the external world, which is set to zero.

2.3.2 Non Lattice Model

The standard cell geometry of MCNP fully describes the location, material, and boundaries of each of the 11025 cells, without using lattices or multiple universe levels. Figure 2.13 shows a portion of the input deck where all planes and cells are listed explicitly.

```
c       cell cards
c
     1    56   -0.12930E-02   111   -112   211   -212   311   -312
     2    56   -0.12930E-02   112   -113   211   -212   311   -312
     3    56   -0.12930E-02   113   -114   211   -212   311   -312
[many cell cards]
11025    56   -0.12930E-02   131   -132   231   -232   335   -336
11026    0            -1000 ( -111:  132: -211:  232: -311:  336)
11027    0    1000
c       BLANK LINE

c       BLANK LINE
c
   111   px    -10.500000
   112   px     -9.500000
   113   px     -8.500000
   114   px     -7.500000
   115   px     -6.500000
[many other px, py, pz planes]
```

Figure 2.13 MCNP non-lattice cells and surfaces.

The non lattice neutron and gamma BNCT problems require forty-six and forty-three Megabytes of RAM, respectively. These memory requirements are large enough to prevent MCNP from operating within a Windows NT DOS window. The standard MCNP4B lattice version decreases these memory requirements to nineteen and fourteen Mbytes, but it prohibitively increases wall clock runtimes, by a factor of about one hundred. The non lattice model capability is useful to retain for running on other platforms, such as UNIX, especially when MCNP cannot be recompiled with time reducing enhancements, and for model visualization with Sabrina. During the Harvard/MIT treatment planning calculations, the lattice model is used exclusively.

2.3.3 MCNP Materials

MCNP requires a description of the matter that fills any location. The materials card provides a description of the isotopes and abundances, as well as the cross section library associated with each isotope. Figure 2.14 is a part of the materials portion of the input deck.

```
m1      1001.50c  -0.1058481   6012.50c  -0.1395953   7014.50c  -0.0184258
        8016.50c  -0.7269170  15031.50c  -0.0039055  17000.50c  -0.0014020
       19000.50c  -0.0039055   5010.50c  -0.0000010
m2      1001.50c  -0.1058481   6012.50c  -0.1395953   7014.50c  -0.0184258
        8016.50c  -0.7269168  15031.50c  -0.0039055  17000.50c  -0.0014020
       19000.50c  -0.0039055   5010.50c  -0.0000012
m3      1001.50c  -0.1058480   6012.50c  -0.1395952   7014.50c  -0.0184258
        8016.50c  -0.7269167  15031.50c  -0.0039055  17000.50c  -0.0014020
           19000.50c  -0.0039055    5010.50c  -0.0000014
       [portion removed]
m52     1001.50c  -0.0499354   6012.50c  -0.1398192   7014.50c  -0.0409527
        8016.50c  -0.4497058  15031.50c  -0.1098579  20000.50c  -0.2097288
m53     1001.50c  -0.1053278   6012.50c  -0.1389091   7014.50c  -0.0221585
        8016.50c  -0.7244360  15031.50c  -0.0038863  17000.50c  -0.0013951
       19000.50c  -0.0038863   5010.50c  -0.0000010
m54     1001.50c  -0.1053277   6012.50c  -0.1389090   7014.50c  -0.0221585
        8016.50c  -0.7244353  15031.50c  -0.0038863  17000.50c  -0.0013951
       19000.50c  -0.0038863   5010.50c  -0.0000020
m55     1001.50c  -0.0498282   6012.50c  -0.1395189   7014.50c  -0.0425352
        8016.50c  -0.4492173  15031.50c  -0.1096220  20000.50c  -0.2092784
m56     7014.50c  -0.7778000   8016.50c  -0.2222000
```

Figure 2.14 Materials Cards in MCNP BNCT treatment planning input deck.

The m1 states that for material one, an isotope with atomic number of one and atomic mass of 001, i.e. ^1H, is present with a mass fraction of 0.1058481, an isotope with an atomic number of 6 and atomic mass of 012, i.e. ^{12}C, is present with a mass abundance of 0.1395953, etc. The ".50c" after each isotope identification indicates that the continuous cross sectional data from the Evaluated Nuclear Data File (ENDF) V library data set, should be used. The minus sign indicates the mass fraction rather than atomic fraction is used. Densities are specified in the cell cards.

As indicated in Chapter two, each of these materials corresponds to a different fractional combination of air, tissue, bone and tumor or other ROI defined region of space. Table 3.1 lists the combination of these in each material.

Table 3.1 MCNP Material Composition Fractions

AIR	BONE	NORMAL TISSUE	TUMOR	MCNP Material
0	0	0	100	1
0	0	20	80	2
0	0	40	60	3
0	0	60	40	4
0	0	80	20	5
0	0	100	0	6
0	20	0	80	7
0	20	20	60	8
0	20	40	40	9
0	20	60	20	10
0	20	80	0	11
0	40	0	60	12
0	40	20	40	13
0	40	40	20	14
0	40	60	0	15
0	60	0	40	16
0	60	20	20	17
0	60	40	0	18
0	80	0	20	19
0	80	20	0	20
0	100	0	0	21
20	0	0	80	22
20	0	20	60	23
20	0	40	40	24
20	0	60	20	25
20	0	80	0	26
20	20	0	60	27
20	20	20	40	28
20	20	40	20	29
20	20	60	0	30
20	40	0	40	31
20	40	20	20	32
20	40	40	0	33
20	60	0	20	34
20	60	20	0	35
20	80	0	0	36
40	0	0	60	37
40	0	20	40	38
40	0	40	20	39
40	0	60	0	40
40	20	0	40	41
40	20	20	20	42
40	20	40	0	43
40	40	0	20	44
40	40	20	0	45
40	60	0	0	46
60	0	0	40	47
60	0	20	20	48
60	0	40	0	49
60	20	0	20	50
60	20	20	0	51
60	40	0	0	52
80	0	0	20	53
80	0	20	0	54
80	20	0	0	55
100	0	0	0	56

Although there are fifty six materials listed, not all of them are significantly different. The difference between materials three and four, one sixty percent tumor forty

percent tissue, and the other forty percent tumor sixty percent tissue, is extremely small. A more significant difference is that only tissue and tumor cells explicitly contain boron, 5010.50c. The last material, fifty-six, is pure air containing only nitrogen and oxygen. Associated with each of these materials, except air, is cross sections adjustment defined by an $S(\alpha,\beta)$ data set for particles of energy below 4 eV. These adjustments represent significant molecular influences on neutron scattering below 2 eV. These adjustments are not available for tissue, but they are available for light water. Specifically, the cross section correction for ^1H in light water is applied, but no modification to ^{16}O is available[12]. The card used to apply the $S(\alpha,\beta)$ adjustments for material 1 is:

```
mt1      lwtr.01t
```

The .01t specifies the temperature of the light water is 300 K. The available $S(\alpha,\beta)$ data are given in Appendix G.II. of the MCNP4B Manual.

2.3.4 Neutron and Photon Source

An accurate representation of the radiation source is essential for proper simulation of an irradiation. The BNCT treatment planning neutron and photon input decks each have detailed source descriptions, representing the irradiation beam as a disk source with spatial, energy and angular distributions. The disk has a specific location and orientation associated with it, which is defined by the medical physicist to have a specific orientation with respect to the patient. While the patient is physically moved to a specific orientation with respect to a fixed radiation beam in the BNCT irradiation, within MCNP, the patient model is fixed and the source is moved.

Within the MCNP input deck, the particle source for the BNCT problems is defined by the sdef card, the general source definition. The variables rad, pos, axs, and ext specify the distribution and locations of source particles. The pos modifier specifies the position of the disk's center, while the axs specifies the vector normal to the disk's surface. Ext is used to determine the distance from the disk's surface a particle is created. The default ext option is zero, indicating the source is a disk source, rather than a cylinder. Rad specifies the radius of the disk. The vec and dir variables specify the range and distribution of the source particle's directions. The

vec modifier specifies the direction the created particle is traveling. Dir specifies the angle or distribution about the vec that particles will be created in. The cosine of this angle is μ. The above variables are illustrated in Figure. 2.15.
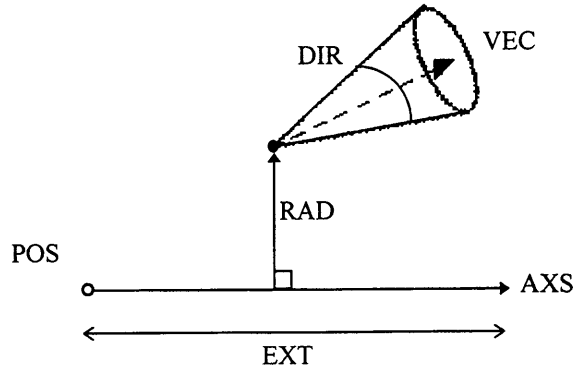
Figure 2.15 Particle Creation Modifiers for a Cylindrical Source. A particle's initial location, indicated by the solid black dot, is described by the specified position (POS), axis (AXS) and radius (RAD). The particle's initial direction is modified by a vector (VEC) and μ (DIR), the angle between the particle's initial direction and the specified vector.

Each of the above variables can be specified by a single discrete value or distribution of values, allowing the user to model complicated distributions in phase space. To specify a distribution, the user sets the variable equal to some distribution, d#. Accompanying si# and sp# cards specify if the distribution is predefined or entered by the user. In several instances, it is useful to correlate distributions. Making one distribution a function of a previously determined variable is done by setting the sdef variable equal to fXXX, where XXX is the independent variable. For example, eng=frad d2 sets the energy for a particular particle equal to a value or distribution depending on what the radius of that particle was determined to be.

The MITR-II M67 epithermal beam is represented as a function of radial position, energy and direction[26,12]. This model of the neutron and gamma component of the beam is based on three radial bins. The angular and energy distributions, having 3 and 93 bins respectively, are each functions of the radial bin, but are independent of each other. This is conceptually illustrated in Fig 2.16.
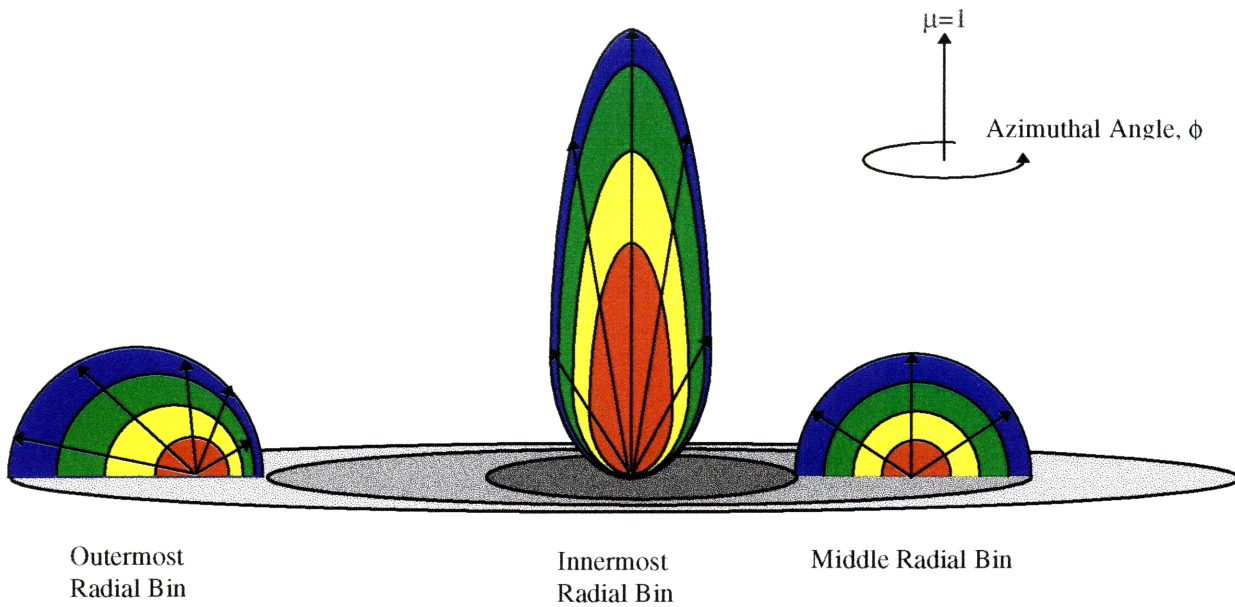
Figure 2.16 Correlated radial and angular distributions in a hypothetical BNCT disk gamma source.
The above figure shows a hypothetical polar plot of the direction and energy distributions for a particle created in the center of a given radial bin. The center bin is foreword peaked, the middle bin is nearly isotropic, and the outer radial bin is greatly outward peaked. The shading of the radial bin is an indication of the relative number of neutrons in that bin. Since the spatial sampling of neutrons within a radial bin was set to be constant in area, the shading throughout a radial bin is constant. The shading of the radial bins indicates that energy distribution is constant within a single radial bin, irrespective of the direction the particle is traveling. The patterns of color are representative of the energy distribution in a bin. Higher energies are represented in red and yellow, while lower energy photons are green and blue.

A significantly improved MCNP neutron source is currently being used[27]. It has correlated energy and angular distributions in each radial bin, in addition to having increased detail of distributions. This is done by spatially superimposing three radial groups, each with one of three energy groups. Each of the nine distinct sources has its own angular distribution. The radial, energy and angular distributions have sixteen, twenty and twenty six bins, respectively. The effect is shown in Fig 2.17, which is different from 2.16 in its energy and radial distributions.
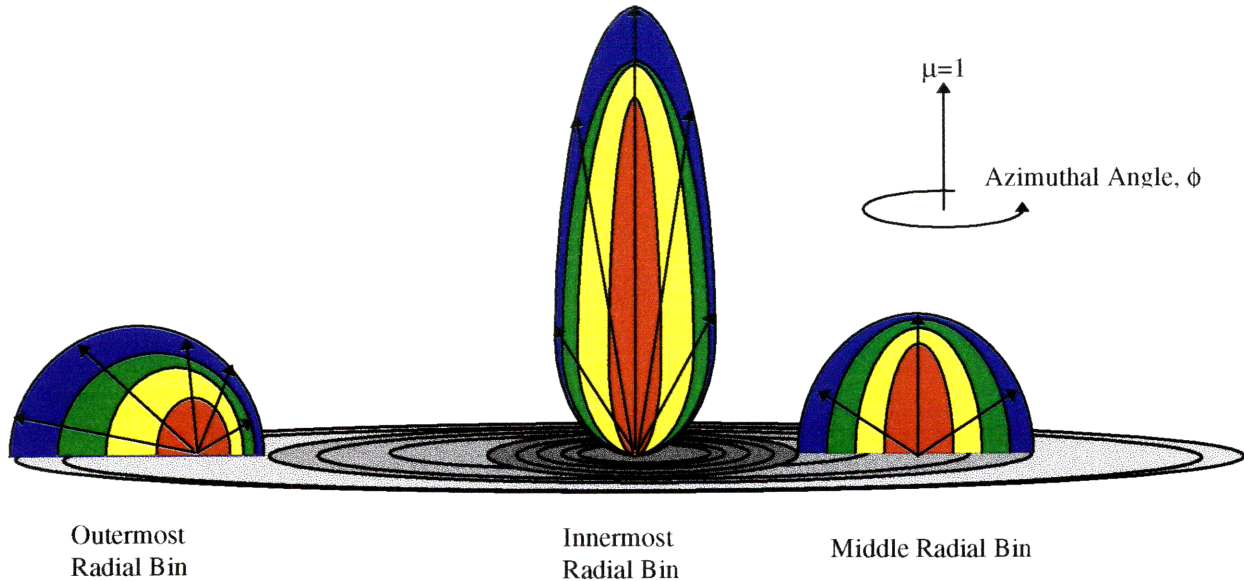
Figure 2.17 Correlated angular, radial and energy distributions in a hypothetical neutron disk source.
The above figure shows a hypothetical neutron source with angular, radial and energy correlations. The length of the black vectors represent the relative number of neutrons going in the vector's corresponding μ direction. The shading of the radial bins indicate that there is a distribution in the 16 radial bins. The patterns of color are representative of the energy distribution in a bin. Higher energies are represented in red and yellow, while lower energy photons are green and blue. The amount of a certain color a black vector passes through is proportional to the probability its energy will be within that energy bin. Four energy bins are shown here.

As shown in Fig. 2.17, the innermost radial bin is greatly forward peaked, and the forward peaked neutrons have a more energetic distribution within that bin, as indicated by the greater proportion of red along the vector of a $\mu=1$ source neutron. The middle radial bin is isotropic for $\mu>0$, as indicated by the constant length of the source particle direction vector in the polar plot. The neutrons traveling perpendicular to the surface of the disk are also more energetic. Conversely, the neutrons traveling more parallel to the surface of the disk, those with $\mu\sim1$, have a more thermal distribution. The neutrons created in the outer energy bin have a higher μ distribution and a more thermal distribution. Those few that are still traveling along $\mu\sim0$ have a higher energy distribution.

2.3.5 Flux Tallies

MCNP can determine a number of quantities of interest. The surface averaged current, surface averaged flux, cell averaged flux, flux at a point or ring detector, the average energy deposited in a cell, or fission energy deposition can all be calculated by using a tally card. These cards include information on what is to be calculated and what cells or surfaces should be used. Since the dose rate averaged over a cell is the ultimate goal for the BNCT treatment planning simulation, the F4:N (or F4:P) card, or cell averaged flux card, is used to find the flux from neutrons and photons respectively. The flux will be multiplied by the energy dependent KERMA to dose conversion factor. When used with the lattice model, the card to calculate the cell averaged neutron flux in every lattice element is:

```
f4:n        (1000<1000[0:20 0:20 0:24])
```

The resulting value is the number of neutron per square centimeter per source neutron. In order to find the dose rate, this value should be convolved with the energy dependent energy deposited per neutron and multiplied by the total neutron current. The tally multiplier card multiplies each cell averaged flux by the number specified. The card shown below will multiply each of the 11025 lattice element "cell" fluxes by 5E11 n/min, which corresponds to the reactor power at 5 MW.

```
fm4        5.00000E+11
```

2.3.6 Flux to Dose Multipliers

MCNP uses the dose energy and dose function cards to convert neutron flux to dose rate. These cards allow the user to enter energy dependent flux multipliers; the Harvard/MIT BNCT treatment planning calculations use Kerma factors. The Kerma factors are different for each dose component, either thermal or fast neutron, photon, or boron. The kerma factors used in our treatment planning runs were calculated were from the cross sections and nuclear reaction data[14]. For convenience, these two cards are entered in column format rather than in rows. The columns must be of equal length and

contain monotonically increasing energies. Figure 2.18 shows a portion of the DE DF cards used to convert the photon fluence into photon dose rates.

```
#              de34           df34
c         Energy (Mev)     Photon Brain Tissue
          1.00e-03          5.45e-08
          1.50e-03          3.00e-08
          2.00e-03          1.83e-08
        [many more entries]
          1.45e+01          3.53e-09
          1.50e+01          3.63e-09
```

Figure 2.18 Dose Cards in MCNP BNCT treatment planning input deck. For energies between listed values, interpolation is log log.

Using the above methods of patient modeling, materials and source description and appropriate tallies and dose conversions, MCNP calculates the dose to every voxel in a simulated irradiation. MCNP is capable of handling the complexities of the irradiation simulation, in addition to giving the knowledgeable user the flexibility to easily make changes to the simulation.

References

1 G.L. Locher, "Biological effects and therapeutic possibilities of neutrons," Am. J. Roentgenol. **36**, 1 (1936).

2. D. Gabel, S. Foster, and R. Fairchild, "The Monte Carlo simulation of the biological effect of the $^{10}B(n,\alpha)^7Li$ reaction in cells and tissues and its implication of boron neutron capture therapy," Rad. Res. **111**, 14-25 (1987).

3. R. F. Barth, A.H. Soloway, and R. G. Fairchild, "Boron neutron capture therapy for cancer," Sci. Amer. 100-107 (October, 1990).

4. R. F. Barth, A. H. Soloway, and R. G. Fairchild, "Boron neutron capture therapy of cancer," Cancer Res. **50**, 1061-1070 (1990).

5. D. E. Wazer, R. G. Zamenhof, H. Madoc-Jones, and O. K. Harling, "Boron neutron capture therapy," Cancer of the Nervous System, 227-245 (1997).

6. R. L. Moss, O. Aizawa, D. Beynon, R. Brugger, G. Constantine, O. Harling, H. B. Liu, and P. Watkins, "The requirements and development of neutron beams for neutron capture therapy of brain cancer," J. Neur. Oncol. **X**, 27-40 (1997).

7. O.K. Harling, P. Busse, R.G. Zamenhof, G. R. Solares, W.S. Kiger III, K.R. Riley, C.F. Chuang, and H. Madoc-Jones, "Long-term clinical followup up of subjects in a BNCT protocol," Trans. Am. Nucl. Soc. **75**, 35 (1996).

8. P. Busse, R. G. Zamenhof, O. H. Harling, I. Kaplan, J. Kaplan, C. Chuang, J. Goorley, W.S. Kiger III, K. Riley, L. Tang, G. Solares, and M. R. Palmer, "Complete response of cutaneous and intracranial melanoma to BNCT," submitted to Eighth Int. Symp. Neut. Cap. Ther. Canc.

9. MIT Nuclear Reactor Laboratory Technical Specifications 6.5. Docket 50-20, Amendment #30 to License R-37 U.S. Nuclear Regulatory Commission (April 3, 1997).

10. W.S. Kiger, III, R.G. Zamenhof, G.R. Solares, E. L. Redmond II, and C.-S. Yam, "MacNCTPlan: An Improved Macintosh-Based BNCT Treatment Planning Program," Trans. Am. Nucl. Soc. **75**, 38 (1996).

11. W.S. Kiger III, "MacNCTPlan user's manual" Version 2.1 Harvard/MIT BNCT Project internal document (1998).

12. R.G. Zamenhof, E. Redmond II, G.R. Solares, D.Katz, S. Kiger, and O.K. Harling, "Monte Carlo based treatment planning for boron neutron capture therapy using custom designed models automatically generated from CT data," Int. J. Rad. Oncol. Biol. Phys. **35**, 383 (1996).

13. J.F. Briesmeister, Ed. "MCNP - a general Monte Carlo N - particle transport code," v. 4B, Los Alamos National Laboratory report LA-12625-M Version 4B (March 1997).

14. R. G. Zamenhof, S. D. Clement, O. K. Harling, J. F. Brenner, D. E. Wazer, H. Madoc-Jones and J. C. Yanch. "Monte Carlo based dosimetry and treatment planning for neutron capture therapy of brain tumors," in *Neutron Beam Design, Development and Performance for Neutron Capture Therapy*, edited by O. K. Harling, J. A. Benard, R. G. Zamenhof. (Plenum, New York, 1990), pp. 283-305.

15. R. D. Rogus, O. K. Harling, and J. C. Yanch, "Mixed field dosimetry of epithermal neutron beams for boron neutron capture at the MITR-II Research Reactor," Med. Phys. **21**, 10 (1994).

16. R. D. Rogus, Ph. D. thesis, "Design and dosimetry of epithermal neutron beams for clinical trials of boron neutron capture therapy at the MITR-II Reactor", Massachusetts Institute of Technology 1994.

17. O. K. Harling, R. Rogus, J. R. Choi, D. J. Moulin, R. G. Zamenhof, and J. C. Yanch. "Dosimetry and dose control for clinical trials of neutron capture therapy at the MITR-II Reactor," International Workshop on Macro and Microdosimetry for Boron Neutron Capture Therapy, (MIT Press, Cambridge, 1991).

18. W. S. Kiger III, K. Riley. Personal communication. Scaling factors for the June 1997 MITR Epithermal Beam Phantom Calibration. November 1997.

19. K. J. Riley, O. K. Harling, "Boron-10 analyses using prompt gamma neutron activation and ICP-AES," Trans. Am. Nucl. Soc., **75**, 31 (1996).

20. W. S. Kiger III, G. R. Solares, C. -S. Yam, K. J. Riley, O. H. Harling, and R. G. Zamenhof, "Boron-10 quantification and microdosimetric studies in a clinical trial of BNCT," Trans. Am. Nucl. Soc., **75**, 34 (1996).

21. O. K. Harling, D. J. Moudlin, J. -M. Chabeuf, and G. R. Solares, "On-line beam monitoring for neutron capture therapy at the MITR-II Research Reactor," Med. Phys. **21**, 10 (1994).

22. G. R. Solares, D. Katz, O. K. Harling, R. Zamenhof, "On-line dosimetry for boron neutron capture therapy at the MIT Research Reactor," Nucl. Instr. Meth. Phys. Res. B. **101**, 464-472 (1995).

23. W. S. Kiger, III. "BNCT Rx manual dosimetry protocol," Harvard/MIT BNCT Project internal document. (1997).

24. L. G. Bouchet, W. E. Bolch, D. A. Weber, H. L. Atkins, and J. W. Poston Sr. "A revised dosimetric model of the adult head and brain," J. Nucl. Med. **37**, 1226-36 (1996)

25. L. G. Bouchet, W. E. Bolch, D. A. Weber, H. L. Atkins, and J. W. Poston Sr. "MIRD pamphlet no. 15: Radionuclide S values in a revised dosimetric model of the adult head and brain" (1998).

26. E. L. Redmond II, J. C. Yanch, and O. K. Harling, "Monte Carlo simulation of the Massachusetts Institute of Technology Research Reactor," Nucl. Tech. **106**

27. W. S. Kiger III, Personal communication. Modifications to the photon and neutron source used in Harvard/MIT BNCT MCNP treatment planning calculations. 1998.

3. Treatment Planning MCNP Run Time Reductions

The preceding chapters describe the typical Harvard/MIT BNCT treatment planning process. Although functional, it was a time consuming process, taking more than three days for each subject. If BNCT is proven to be effective and integrated into mainstream medical therapies, the procedure must be much more time efficient. Since the Monte Carlo dose rate calculations accounted for two to three days of the process, it was targeted for optimization. Three approaches for run time reduction were investigated: use of an appropriate number of source particles, MCNP4B[1] source code modifications and parallel computing. After verifying that the appropriate number of source particles were being used with a voxel statistical error analysis described later, the MCNP4B source code was modified by LANL personnel to decrease the runtime of a lattice problem by a factor of nearly one hundred, although the resulting speedup was only faster than the non lattice version by a factor of two. This enhanced version was also modified to run in parallel, allowing factors of speedup roughly equal to the number of computers used. The implementation and description of these three approaches are described in sections 3.1, 3.2 and 3.3, while their verification is described in the last section, 3.4.

Additional improvements were made to the BNCT dosimetry procedure, after the discovery of a new phenomenon. When the time of the second beam of a two beam irradiation was increased beyond the first irradiation duration, caused by unexpected complications in the first beam irradiation, the maximum dose location moved. This movement placed the maximum dose location in a much higher dose rate location, leading to an underestimation of the delivered dose. To anticipate this effect in the future, a table of dose rate contributions from various weighted beams can be generated using existing capabilities within MacNCTPlan, which are currently used to find the dose rate contributions for the anticipated treatment plan. This research is described in chapter three of this thesis.

The final improvements from this thesis are the volume dosimetry calculations, which include calculating the dose volume histograms and volume average doses for tumor and normal tissue. The subject's dose volume histograms depend on the geometric combination of the irradiation beams and dose cohort grouping. An analysis of the subject volume doses leads to a proposed alternative cohort grouping.

3.1 Uncertainty Analysis

The first obvious means of reducing the runtime of the beam calculations is to reduce the number of source particles. While this will increase the error associated with the dose rates calculated, it may still be within acceptable bounds. For example, in scoping runs, if only a rough distribution of dose in the target body part is needed, or if only a high dose rate regions near the tumor are important, then the uncertainty in unimportant regions could be allowed to grow large, requiring fewer particles and decreasing run times. If the treatment employs parallel opposed beams, where a beam is used to increase the dose rate to the deep side of the tumor by passing through the bulk of the body part, a larger number of particles needs to be run to accurately evaluate the effect of the second beam at that distal location. The effects of number of particle histories on statistical uncertainty of the voxel dose rates and the isodose rate contours were investigated.

3.1.1 Voxel Dose Uncertainty Analysis

Total dose rates are the sum of five dose components, fast and thermal neutron, structural and induced gammas, and boron. Each of these is product of the Relative Biological Effectiveness (RBE), scaling factors, the boron concentration for the boron component, and the physical dose rates calculated by MCNP. The relative error for the total dose rate for each voxel is determined, via propagation of error, from the relative uncertainty provided by MCNP for each dose rate component. Based on the error propagation formula, equation 3.1, and the equation for the total dose rate, equation 3.2, the total statistical dose rate error is shown in equation 3.3.

$$\sigma^2_{DRTotal} = \left(\frac{\partial DR_{Total}}{\partial DR_{FN}}\right)^2 \sigma^2_{DRFN} + \left(\frac{\partial DR_{Total}}{\partial DR_{TN}}\right)^2 \sigma^2_{DRTN} + \left(\frac{\partial DR_{Total}}{\partial DR_B}\right)^2 \sigma^2_{DRB}$$

$$+ \left(\frac{\partial DR_{Total}}{\partial DR_{IG}}\right)^2 \sigma^2_{DRIG} + \left(\frac{\partial DR_{Total}}{\partial DR_{SG}}\right)^2 \sigma^2_{DRSG}$$

Equation 3.1.

$$DR_{Total} = a_{FN}DR_{FN} + a_{TN}DR_{TN} + a_B DR_B + a_{IG}DR_{IG} + a_{SG}DR_{SG}$$

Equation 3.2.

$$\sigma_{TDR}(i) = \sqrt{\sum_{f=1}^{5}\left(a_f \zeta_f(i) D_f(i)\right)^2}$$

Equation 3.3.

The total dose rate error for a specific voxel, σ_{TDR} (i), is the absolute computed uncertainty (1σ) for the total dose rate, in RBE cGy, to voxel i. The relative Monte Carlo uncertainty calculations by MCNP for voxel i and component f is represented as ζ_f (i). The dose rate is represented by $D_f(i)$. The product, $\zeta_f D_f$, is the error, σ_f, for each voxel.

The above equations neglect the uncertainty in the RBE, boron concentration, and scaling factors, which is substantial, but is not well known. The relative total dose rate error is the absolute dose rate error divided by the total dose rate, and is plotted as a function of number of source particles and dose rate in Fig. 3.1.
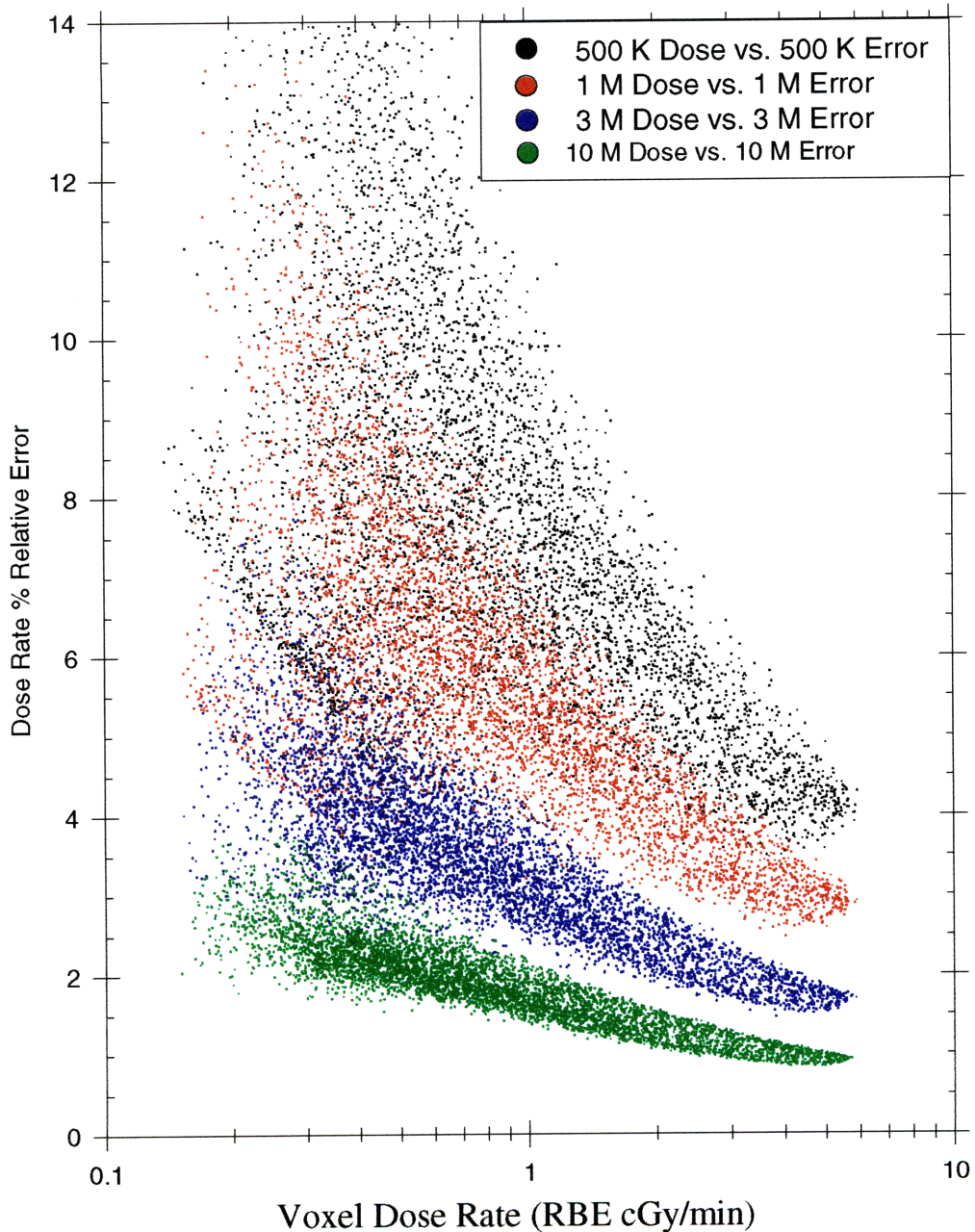
Figure 3.1. Total dose rate uncertainty for various number of histories

Figure 3.1 shows the total dose rate relative error associated with every non air containing cell for runs of five hundred thousand, one, three and ten million particles. The high dose rate cells have the lowest relative error, while the lower dose rate regions have larger errors. The results of this graph show the reduction of total dose rate uncertainty as the number of particles increases.

On Fig. 3.1, the appropriate number of source particles for various treatment plans can be determined qualitatively. For single beam irradiation scoping runs, where only high dose rate cells will be contributing to the tumor dose, only the higher dose rate cells will need to be determined to 5% error. Figure 3.1 shows the dose rates to a region receiving 1-2 RBE cGy/min with an uncertainty of 5% or less occurs roughly between 500,000 and 1,000,000 histories. For dual beam irradiations, where 0.5 to 1 RBE cGy/min would be contributed to the tumor from the second beam, between one and three million particle should be used in the scoping runs to obtain less than 5% uncertainty. Figure 3.1 also shows that for dose volume histograms, where the dose throughout the entire volume of neural tissue should have little uncertainty, ten million histories should be run.

An analysis of the statistical uncertainty and the number of particles used shows an agreement with the one over square root of N statistical law. For the highest dose rate cell, the uncertainty associated with five hundred thousand particles is nearly 5%. When a factor of twenty more particles are run, the uncertainty should be reduced by a factor of one over 4.47, in close agreement to the 1% uncertainty of the error.

3.1.2 Isodose Rate Contour Analysis

While figure 3.1 may give a clear understanding of the error associated with certain dose regions, the actual pictures from the isodose rate contours in MacNCTPlan provide a different perspective. While the images do not incorporate the total dose rate error, they will show the fluctuations of the total dose rates with the number of particles. Figures 3.2 a-e show the MacNCTPlan isodose rate contours for the same subject and beam orientation, but with different number of histories.
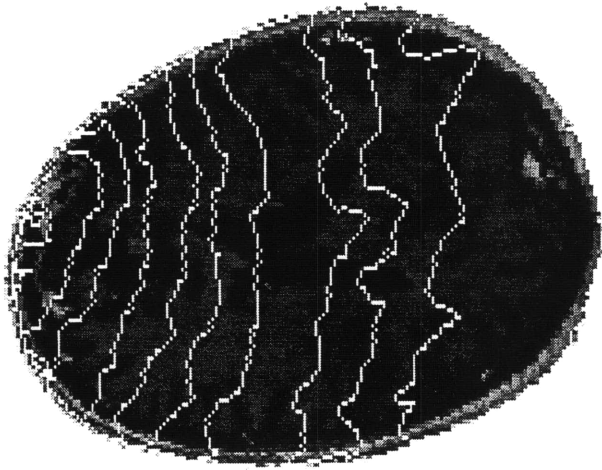
Figure 3.2 a.
Subject 97-3 Two Hundred Fifty Thousand Particles
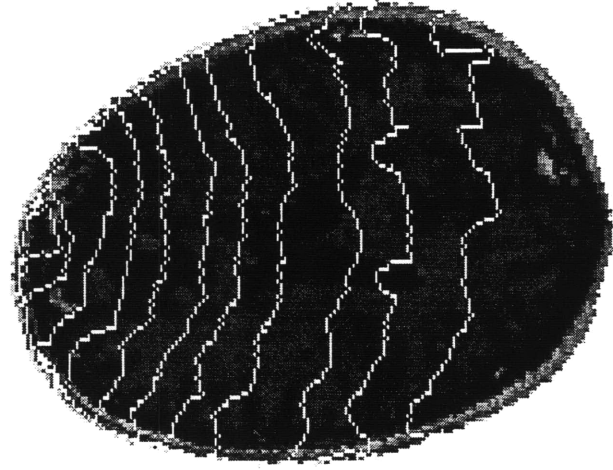
Figure 3.2 b
Subject 97-3 Five Hundred Thousand Particles
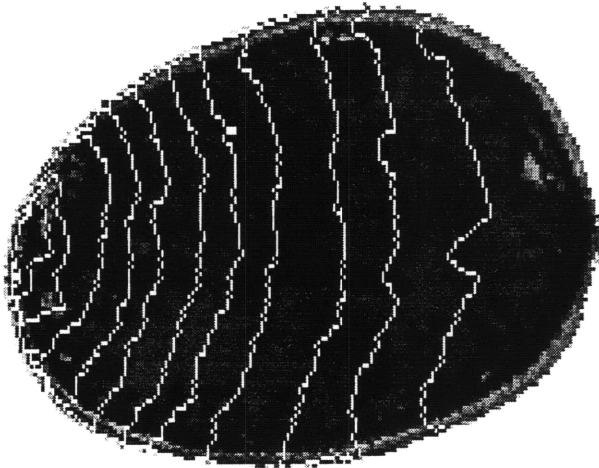
Figure 3.2 c.
Subject 97-3 One Million Particles
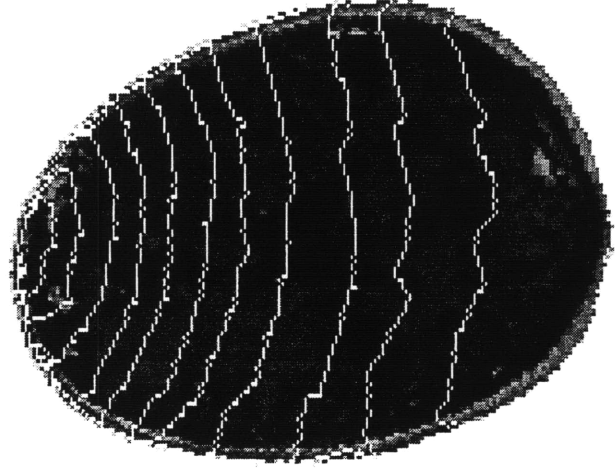
Figure 3.2 d
Subject 97-3 Three Million Particles
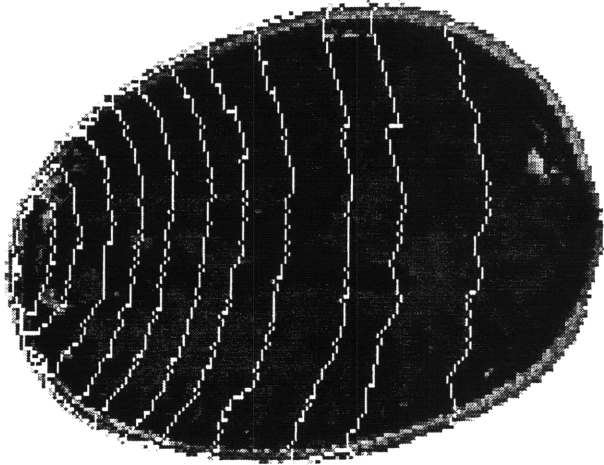
Figure 3.2 e.
Subject 97-3 Ten Million Particles

The above figures show the isodose rate contours from a single irradiation beam entering from the left. The contours outline the following fractional dose rates from the peak dose rate: 95, 90, 80, 70, 60, 50, 40, 30, 20, 15, 10, 5.

The above images, all of the same cross section of the same subject, illustrate several points. The high dose rate region gradually increases by ten percent in dose and physical size as the number of particles increases. All contours become less erratic and more representative of a continuous dose distribution as the number of particles increases. The two lowest trials (Fig 3.2 a,b) also have the bottom edge of the tumor in an isodose rate region five percent lower than the final ten million history run (Fig 3.2e).

A quick comparison between the error estimates and the isodose rate contours show that the error restrictions are the more restrictive of the two. If the number of histories needed to be run was based on the isodose rate contours only, the number of histories would be too few by almost a factor of two. As seen in fig 3.2e, the tumor receives forty-five percent of the maximum dose at its lowest point, or roughly 2.7 RBE cGy/min. On Fig 3.1, which is derived from the same subject MCNP data, the error associated with the one million history runs, for voxels receiving a dose rate of 2.7 RBE cGy/min or higher, is within five percent. From figures 3.1a-e, the tip of the tumor would be within five percent of its final value somewhere between one million and five hundred thousand. The scoping run for this subject was one million particles.

For the ten million history final run, the errors are much less. The statistical error is within two percent in the regions of interest and within three percent for almost all voxels. The isodose curves are smooth and well defined.

Since the number of particles cannot be reduced further without unacceptable increases in statistical uncertainty, additional methods of reducing the run times were investigated.

3.2 MCNP Source Code Improvements

Several modifications were made to the source code by Los Alamos National Laboratory to increase the quality and speed of MCNP. MCNP4B was released February 1997, adding several improvements over MCNP4A[2]. While no changes were made to the neutron and gamma transport physics, the electron physics was improved. Other improvements allow greater flexibility, such as differential operator perturbations and improved cross section plotting features. While the unmodified MCNP4B does run slightly slower than MCNP4A, source code enhancements by Los Alamos National Laboratory personnel removed unnecessary features and tailored the MCNP4B executable for Harvard/MIT BNCT treatment planning calculations, greatly increasing the executable's speed. As part of this thesis, these changes were verified and implemented in the HARVARD/MIT Treatment Planning procedure. Utilization of recently released FORTRAN compilers with better optimizing features also decreased executable runtimes.

3.2.1 Tracking and Tally Patch

The MCNP source code can be greatly optimized for certain lattice problems. Tracking and tallying optimizations were developed for the Harvard/MIT BNCT treatment planning problem by Dr. Gregg McKinney and Dr. Ken Adams of LANL. The tally optimization removes extraneous energy bins and tally modifiers, while retaining the necessary tally multipliers and DE, DF cards that are used to convert volume averaged neutron fluxes to dose rates. Tracking was made more efficient by removing checks for

generalized geometries and specifying that the voxels are enclosed by hexahedra. These tracking and tally enhancements can be applied to the MCNP4B source code with a patch file and the standard compilation procedure to create a specialized MCNP executable called MCNPBNCT. These optimizations reduce the runtimes by factors of two for the tracking modifications and fifty for the tallying modifications over the standard MCNP4B code[3]. This reduces the execution times of the lattice model below that of the standard cell model, as shown in table 3.2 Furthermore, MCNPBNCT is compatible with the Parallel Virtual Machine (PVM) multiprocessing code, allowing for further reductions in runtimes.

Table 3.2 MCNP Wall Clock Run Times (min : sec)

	NPS=10,000		NPS=1 M	
	Neutron	Gamma	Neutron	Gamma
Lattice (NT)	503:56	71	51,000*	6,885*
Lattice w/ Enhancements (NT)	3:44	2:10	54:00	5:18
Lattice (Linux)	848:05	8:43	85,000*	341*
Lattice w/ Enhancements (Linux)	4:23	3:14	81:35	5:53
No Lattice (Linux)	19:18	5:50	199:53	51:03

The astrix denotes an estimated time, in minutes, the other values are measurements. Since the non-lattice input deck would not run under NT, it was run under Linux.

3.2.2 Lahey FORTRAN 90

MCNPBNCT was compiled using the Windows version of the Lahey FORTRAN 90 compiler, LF90. It uses more efficient optimizations to create an executable ten to fifteen percent faster than the previously used compiler, Lahey FORTRAN 77. The primary disadvantage is the slow response to user interrupts (i.e., control-c) of the LF90 compiler, requiring the user to wait five to ten minutes before he or she can quit MCNP, rather than after a few seconds with the F77 compiler.

3.2.3 GNU G77

An alternate compiler investigated was the GNU G77 compiler. The GNU suite of tools, including FORTRAN and C compilers, as well as networking and system tools, works under a variety of platforms, including Linux, UNIX and Windows. The GNU compiler was used to compile MCNP on a PC running Linux. The resulting executable was roughly ten percent slower than the LF90 on Windows. Since the operating systems also changed, the runtime reduction attributed to the compilers themselves should not be compared, only the final runtimes of the executables they create.

The combination of compiling with the Lahey F90 compiler and source code enhancements reduced the wall clock runtimes to thirty percent of the previously used executable. Although this advantage was significant, more dramatic improvements were made by running MCNP in parallel.

3.3. Parallel Calculations

A principal method of MCNP speedup involves the utilization of additional CPU's. While the ability to run MCNP in parallel existed in MCNP4A, it was primarily implemented on architectures other than PC's (i.e. UNIX, SGI). MCNP utilizes the computer program PVM, developed by Oak Ridge National Laboratories, to spawn subtasks and pass messages between a linked network of heterogeneous computers[4,5,6]. Since each source particle history is independent of the previous history, with the exception of the beginning random number used, Monte Carlo transport problems are readily adapted for running simultaneously over multiple CPUs.

Since the Harvard/MIT team previously ran MCNP treatment planning jobs individually on two Pentium Pro 200 MHz computers, the parallel capability of these computers was investigated. Previous efforts to link IBM personal computers such as these and run MCNP have centered on Linux. Cameron Kellough tested MCNP4A in parallel on PC's running Linux in the summer of 1996[7], but no one had tested MCNP4B in parallel on PC's. In addition to the new version of MCNP that had been released since his work, the Linux kernel, GNU C compiler, and GNU FORTRAN compiler had all

undergone upgrades. The successful installation of the parallel version of MCNP is detailed in section 3.3.3. Installation attempts on other operating systems, including Windows, Linux-pmac and MkLinux are described in the Appendix A.

3.3.1 Linux Installation

Linux installation and testing was performed on several computers both at Los Alamos and MIT. Each institution had two Micron Pentium Pro computers with 200 MHz processors and a single Sager 166 MHz Pentium laptop. Linux installation was successful with both Red Hat and Slakware Linux distributions. Both include the necessary networking tools needed for PVM. After installation, the Linux kernel was rebuilt for each machine to account for differences in the network cards. After Linux was installed, MCNP4B was installed and tested, as well as the required cross section libraries. The final MCNP4B Linux executable was able to pass all of the test problems except one. The verification of MCNP4B and MCNPBNCT is discussed in section 3.4.

3.3.2 PVM Installation

The several recent releases of PVM can be obtained via anonymous ftp to netlib2.cs.utk.edu. PVM was then installed on each machine, by decompressing the downloaded file and typing "make pvm." The environmental variables PVM_ROOT and PVM_ARCH were set, and the PVM directory, pvm3/bin/Linux was created in the users home directory. Appropriate remote permissions were set by adding the user's name to the .hosts file in his home directory. After starting PVM by typing "pvm" and adding remote machines with the "add" command, pvm was tested. The PVM test problems, such as "hello" and "hello_other", which test remote execution of programs on other linked computers, were used to verify the functionality of PVM.

3.3.3 MCNP Parallel version

MCNP4B was remade with PVM options and linked to the PVM libraries, creating a parallel version of MCNP, "mcnp.pvm"[8]. This version was tested with a test

set of problems designed for multitasking. The final Linux pvm enabled MCNP4B executable performed well, only failing two checks out of twenty nine. To further verify its results, a BNCT treatment planning run was compared with results from the original version. All verification efforts are described in section 3.4.

3.3.4 Speedup Results

Running MCNPBNCT on the Linux operating system on two Micron 200 MHz Pentium Pro computers, the decrease in wall clock times over the previous version, MCNPNEDH, is significant. Table 3.3 shows the improvement for various numbers of histories run.

Table 3.3 Wall clock run times, in minutes, for a single beam evaluation

Number of Particles Tracked	MCNPNEDH	MCNPBNCT w/ PVM
250,000	45 (0.8 hrs)	23 (0.4 hrs)
500,000	87 (1.5 hrs)	34 (0.5 hrs)
1,000,000	150 (2.5 hrs)	59 (1.0 hrs)
3,000,000	507 (8.5 hrs)	172 (2.8 hrs)
10,000,000	1441 (24 hrs)	534 (8.9 hrs)

The number of particles refers to both the number of source photons and neutrons. The times given are actually the sum of these two separate runs.

The combination of the tracking and tallying enhancements and PVM significantly reduced wall clock runtimes. The single beam scoping evaluation of both the neutron and gamma components, previously totaling one hundred fifty minutes on one 200 MHz Pentium Pro running MCNPNEDH, was reduced to fifty nine minutes using two 200 MHz Pentium Pros. The runtimes for MCNPNEDH, MCNPBNCT with the lattice and non lattice geometry, and the PVM enabled MCNPBNCT lattice model with two 200 MHz Pentium Pro's are shown in Figure 3.2
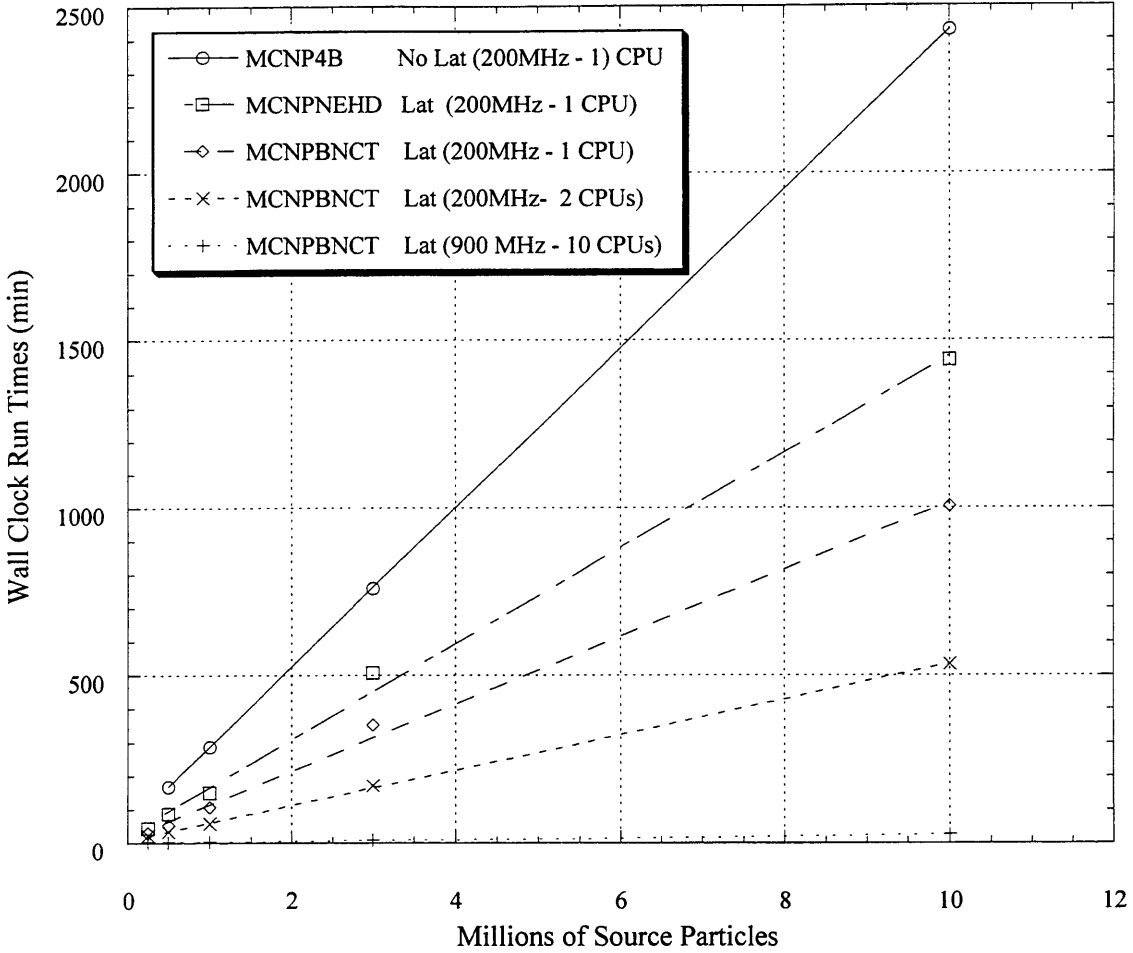
Figure 3.3. Total wall clock runtimes for a single beam evaluation. The uncertainty associated with each point is less than three minutes, i.e. background operating system processes will negligibly affect the runtimes. The numbers in parentheses in the key are how many CPUs were added to the virtual machine.

Since the speed gain associated with running in parallel is a factor roughly that of the number of computers used[9,10], the time for a single task could be reduced significantly. The estimated effects of adding two and eight additional 200 MHz Pentium Pro computers of equal power to the virtual machine are shown in Table 3.4

Table 3.4 MCNP Speedup Summary - Total Wall Clock Runtimes

Source Particles Tracked	MCNPNEDH 1 CPU min (hrs)	MCNPBNCT 2 CPU's min (hrs)	MCNPBNCT 4 CPU's* min (hrs)	MCNPBNCT 10 CPU's min (hrs)	MCNPBNCT 10 CPU's min (hrs)
250,000	45 (0.8)	23 (0.4)	15 (0.2)	9 (0.2)*	2 (0.03)**
500,000	87 (1.5)	34 (0.5)	20 (0.3)	12 (0.2)*	3 (0.05)**
1,000,000	150 (2.5)	59 (1.0)	33 (0.5)	17 (0.3)*	4 (0.07)**
3,000,000	507 (8.5)	172 (2.8)	89 (1.5)	39 (0.7)*	9 (0.15)**
10,000,000	1441 (24)	534 (8.9)	270 (4.5)	112 (1.9)*	25 (0.4)**

A *,** indicates that the times are estimates, not measurements. *Estimates are based on proportional decrease in MCNP ctm time, while startup times remain the same. **Estimates are also based on proportional decreases in total computing time, due to increase in processor speed.

These projected times show that efficient treatment planning beam evaluations can be achieved, minimizing scheduling conflicts and possibly allowing real time treatment planning. An anticipated future project will allow MCNPBNCT to be run in parallel over ten 900 MHz CPUs. This will lower the calculation time to minutes, as shown in the last column of table 3.2.

3.3.3 Running MCNP in Parallel

After PVM was installed on both Linux computers, the parallel version of MCNPBNCT was tested and verified. Afterward, the combinations of multitasking parameters and computational power were studied. Total runtimes were evaluated using a heterogeneous computing network. Even though a single treatment planning beam evaluation will be completed in the least amount of time by using PVM, the BNCT treatment planning process requires the optimization of several beams, which is most efficiently done by running each beam without PVM, when the number of beam evaluations exceeds the number of available computers.

The parallel version of MCNP4B has the ability to perform load balancing[8]. The master MCNP executable, which is the one started by the user, identifies the number of subtasks to be started from the command line option "tasks #". The number entered can be larger than, smaller than, or equal to the number of computers in the virtual machine. The master task starts the subtasks sequentially using the PVM listing of potential hosts

in the virtual machine. If a negative number for the tasks option is entered, an equal number of particles is run on all computers. A positive number will cause the master to evaluate the computing power of all hosts with a limited number of particles. Both options cause the slave subtasks to rendezvous with the master and relay to it the appropriate information. If any of the subtasks have shutdown, the master identifies the discrepancy and runs those particles. The frequency of rendezvous is controlled by the fifth option on the MCNP PRDMP (print dump) card. The PVM load balancing requires computational overhead, which is not needed on a homogeneous computing network. The MCNP command line option "tasks -2" prevents this PVM optimization[1,8], and hence is the best method for running in parallel on the Harvard/MIT BNCT homogeneous network.

3.3.4 Job Identification and Importance

Analysis of the run time reduction due to PVM shows that although the use of PVM does allow a single run to be completed much faster, it is not always an efficient method of running multiple jobs. A pictoral representation is shown in Fig. 7.1 a-d. Since there is some computational overhead from running PVM, using it will add to the total computing power needed for the job. Speedup derives from the division of this total computing power among all CPUs in the virtual machine. This results in a wall clock runtime that is faster than the time for one job to be run on one computer. Figure 3.4 shows the PVM overhead and the reduction in wall clock times. If, however, several jobs need to be run, and the number of jobs equals or exceeds the number of linked computers, then each job should be run on only one computer to eliminate the overhead associated with PVM, as illustrated in Figs 3.4c and 3.4d.
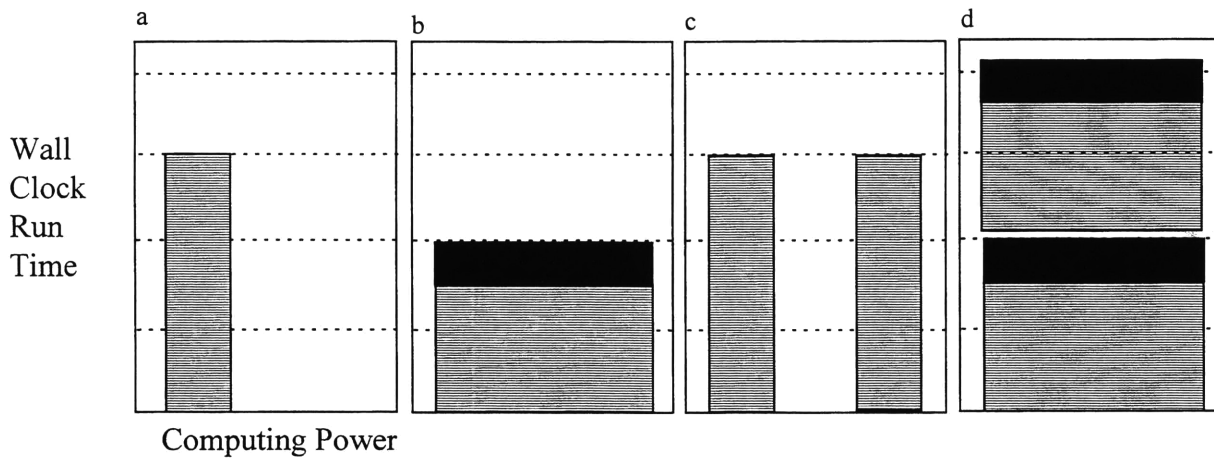
Figure 3.4(a-d). Representation of Jobs and Optimization. Fig. 3.3a represents a single job being run on one computer. Fig. 3.3b represents that same job being run on two computers with PVM. The second smaller dark box on top is the computational overhead associated with PVM. Fig. 7.1c represents two identical jobs being run on two computers without PVM. No additional overhead occurs, nor is the wall clock time greater than in Fig. 7.1a. Fig. 7.1d show two jobs being run with PVM on two computers. The total wall clock time is greater than in 7.1c. due to the PVM computational overhead. The above figures exaggerate the PVM computational overhead, for illustration.

For the BNCT treatment planning scoping evaluations, two single one million source particle tasks (Fig. 3.4c) can be completed in one hour ten minutes, while two sequential jobs, each run in parallel (Fig 3.4d) would be completed in one hour fifty nine minutes. This difference is especially large since the parallel version would be run under the slightly slower Linux operating system, effectively increasing the computational overhead. For a final single beam, however, it is faster to run one job in parallel over the two Pentium pros, as in Fig. 3.4b. The addition of five computers would make running in parallel slightly more efficient for scoping runs, where each job would be distributed over two computers, and significantly more efficient for the final run, where one or two jobs could each be distributed among three or four computers.

3.4 Validations of calculation enhancements

The implementation of the new source code, MCNPBNCT, requires verification before it can be used in treatment planning. Verification consists of two distinct procedures, quality assurance on the code executable and a comparison of the code results to MCNPNEDH.

3.4.1 MCNP4B Test Suite

LANL has several methods for testing and verifying the MCNP source code[11,12]. Included in these is the extensive testing of the source code through the use of twenty-nine test problems. These test problems are run by the newly created executable and compared with expected results. The scripts runprob and runprobmt verify the standard and PVM versions of the executable. Both of these scripts should reference the DOS MCTL and OUTP files, which need to be uncompressed on a DOS machine and transferred via ASCII FTP to the Linux system. These scripts will compare the tally output of the test problems to the reference tally output, the MCTAL files, using the command "diff," which performs a line by line file comparison.

Unfortunately, the test suite utilizes portions of the code that were removed to create MCNPBNCT, so it will not run the enhanced source code. Since MCNP4B had not been verified on Linux, its validation was still important. When MCNP4B is run without PVM, only one non-zero difference file, difm12, is created for the twelfth test problem. It indicated that a different number of random numbers was used during this execution than was used in the reference execution. This inconsistency may be attributed to differences in the Lahey F77 and GNU F77 compilers. When run using PVM, four non zero difm files will be created. Two of them, inp12m and inp08am, do not track. The other two, inp21am and inp28m, result from output differences caused by PVM's rendezvous procedure, which is acceptable. Table 3.5 summarizing the difference files, difm12, difm21a, and difm28, and the files themselves. Difm08a, beyond the header, is too extensive to include here.

Table 3.5 Non-Zero Difm Files from MCNP4B on Linux.

-O0 Optimization	w/o PVM (runprob)		w/ PVM (runprobmt)	
File	Size (bytes)	Error	Size (bytes)	Error
difm08a	N/A	N/A	2669	tracking
difm12	128	tracking	3508	tracking
difm21a	N/A	N/A	1276	rendezvous
difm28	0	none	698	rendezvous

The above files were created when MCNP was compiled with -O0 optimization.

Difm08a header - 2669 bytes
```
1c1
<                                            2       1579         21050
---
>                                            2       1570         19337
```

Difm12 - 146 bytes
```
1c1
<                                            2       3000         4774870
---
>                                            2       3000         4774894
```

Difm21a - 1276 bytes
```
273c273,274
< tfc    10       1       1       22      1       1       1       23
1
---
> tfc    20       1       1       22      1       1       1       23
1
>         1000    4.09176E-05     3.71303E-01
274a276
>         3000    4.08754E-05     1.78175E-01
275a278
>         5000    4.55530E-05     1.68729E-01
276a280
>         7000    4.26109E-05     1.35474E-01
277a282
>         9000    4.09342E-05     1.15212E-01
278a284
>         11000   4.71283E-05     1.23183E-01
279a286
>         13000   4.66970E-05     1.11987E-01
280a288
>         15000   4.50165E-05     1.04542E-01
281a290
>         17000   5.70298E-05     2.23201E-01
282a292
>         19000   5.48663E-05     2.07877E-01
298c308,309
< tfc    10       1       1       1       1       1       1       4
1
---
> tfc    20       1       1       1       1       1       1       4
1
>         1000    4.09176E-05     3.71303E-01
299a311
```

```
>           3000    4.08754E-05   1.78175E-01
300a313
>           5000    4.55530E-05   1.68729E-01
301a315
>           7000    4.26109E-05   1.35474E-01
302a317
>           9000    4.09342E-05   1.15212E-01
303a319
>          11000    4.71283E-05   1.23183E-01
304a321
>          13000    4.66970E-05   1.11987E-01
305a323
>          15000    4.50165E-05   1.04542E-01
306a325
>          17000    5.70298E-05   2.23201E-01
307a327
>          19000    5.48663E-05   2.07877E-01
```

Difm28 - 689 bytes

```
475,476c475,477
< tfc     9        1        1        42       1        1        1        43
1
<           3000    4.92945E-05   6.68206E-01
---
> tfc    13        1        1        42       1        1        1        43
1
>           2000    6.53503E-05   7.50077E-01
>           4000    5.91882E-05   4.71549E-01
478c479,480
<           9000    6.80561E-05   3.98976E-01
---
>           8000    7.29853E-05   4.17453E-01
>          10000    6.23468E-05   3.92323E-01
480c482,483
<          15000    5.00067E-05   3.34972E-01
---
>          14000    5.30353E-05   3.38257E-01
>          16000    6.61325E-05   3.71568E-01
482c485,486
<          21000    6.19494E-05   3.09465E-01
---
>          20000    5.87871E-05   3.36357E-01
>          22000    5.99188E-05   3.05517E-01
```

The above differences were created with a compilation of MCNP without optimization. Although zero optimization produces the fewest number of difm files, runtimes can often be considerably reduced at higher optimizations. When the -O2 optimization is enabled, several difm files are created when runprob and runprobmt are run, as listed in table 3.6.

Table 3.6 Non-Zero Difm Files from MCNP4B -o2 on Linux

-O2 Optimization	w/o PVM (runprob)		w/ PVM (runprobmt)	
File	Size (bytes)	Error	Size (bytes)	Error
difm08a	N/A	N/A	2669	tracking
difm12	3508	tracking	3508	tracking
difm21a	N/A	N/A	1276	rendezvous
difm28	0	none	698	rendezvous
difm29	1686	tracking	1686	tracking
difm29a	N/A	N/A	1686	tracking

The above files were created when MCNP was compiled with -O2 optimization.

There are also CPU specific optimizations. The -m486 option is optimization for the 486. The optimization for the Pentium is: -O2 -m486 -malign-loops=2 -malign-jumps=2 -malign-functions=2. There currently is no specific optimization for the Pentium Pro. The differences between the 486 options and the Pentium options on a Pentium Pro machine are negligible. Since optimizations above -O0 cause more problems not to track, they clearly change answers and thus are officially unacceptable to LANL. Essentially the different number of random numbers being used indicates that either a compiler or hardware error exists that may affect results for particular features or subroutines within the MCNP source code. Since the treatment planning jobs may not use the erroneous routines, it was compared with the previous executable used.

3.4.2 MCNPNEDH MCNPBNCT Dose Rate Comparison

To verify the new code on Linux, a treatment planning calculation for one of the previously subjects enrolled in the Harvard/MIT BNCT study was run using MCNPBNCT in parallel and compared to the previous version, MCNPNEDH. This final beam run used ten million source neutrons and ten million source photons, creating a well converged result with small Monte Carlo uncertainties. Figure 3.4 compares the dose rates in all non-air cells calculated by MCNPBNCT and MCNPNEDH.
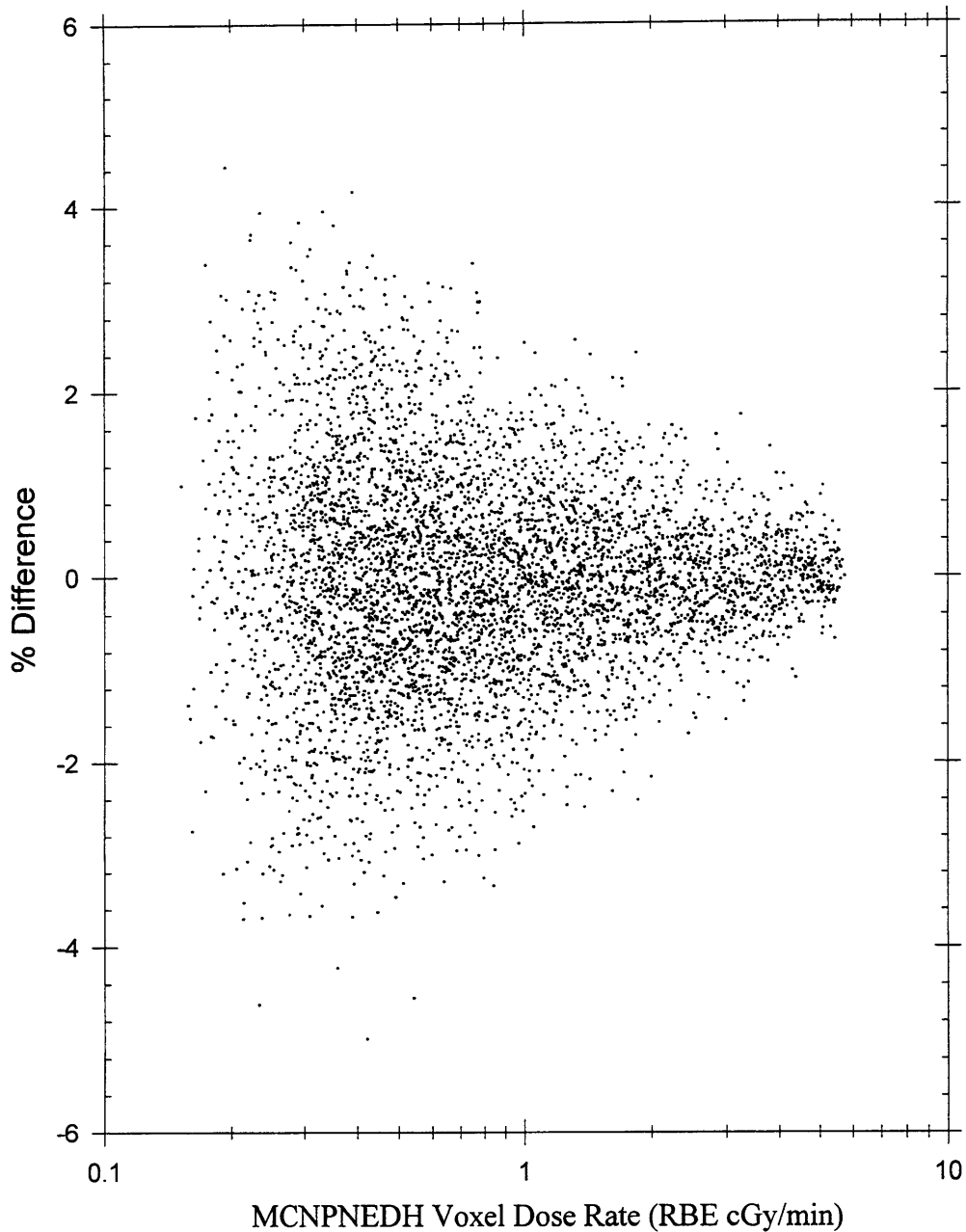
Figure 3.5 MCNP Dose Rate Comparison. Each point represents the difference for a single voxel.

Figure 3.5 shows the percent difference* in results between the previously used MCNP version, MCNPNEDH and the final enhanced pvm version, MCNPBNCT, decrease as dose increases. Even the lowest dose rate cells differ by no more than 5%. This shows

---

* % Difference(i) is 200*[MCNPNEDH DR(i)-MCNPBNCT DR(i)]/[MCNPNEHD DR(i)+MCNPBNCT DR(i)], where DR(i) is the dose rate for the ith voxel.

that the new version of MCNP is acceptable and can be relied on to reproduce the results of the previous version.

Another way of looking at the data is to compare the difference between values calculated by each of the two versions for the same voxel and their error bars. Figure 3.6 shows these data, in addition to a line that indicates that the error bars of a single voxel are the same size as the difference between the two values for the same voxel.
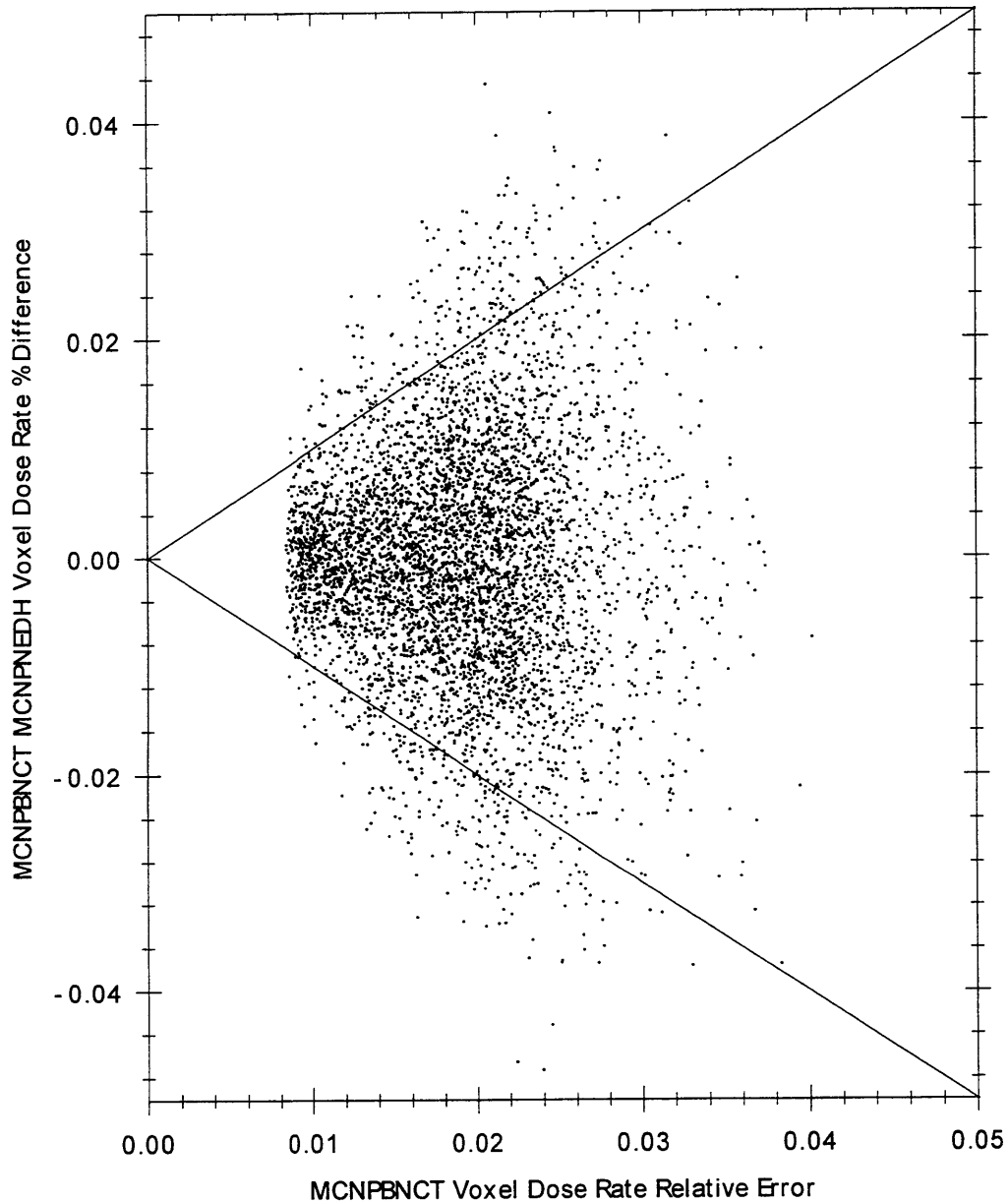
Figure. 3.6 Comparison of Error for each non-air voxel. Each point represents a single voxel dose rate comparison.

If most of the points were inside these lines, this would indicate the values were converging. Since they are, this further validates that the two programs would yield the similar dose rates for identical patient models and particle sources.

References

1. J. F. Briesmeister, Ed. "MCNP - A General Monte Carlo N -Particle Transport Code," v. 4B, Los Alamos National Laboratory report LA-12625-M Version 4B (March 1997).

2. J. S. Hendricks, J. D. Court, "MCNP4B Verification and Validation" Los Alamos National Laboratory Report LA-13181. (August 1996).

3. K. Adams, and G. W. McKinney, Personal communication. The runtime reductions associated with the Los Alamos MCNP patches. (November 1997).

4. A. Geist, A. Beguelin, J. Dongarra, R. Manchek, W. Jiang, and V. Sunderam, "PVM: Parallel Virtual Machine - A user's guide and tutorial for networked parallel computing" Cambridge, MA. The MIT Press. (1994).

5. V. S. Sunderam, "PVM: A Framework for Parallel Distributed Computing," Concurrency: Practice and Experience, 2, 4, 315-339 (December 1990).

6. J. Dongarra, A. Geist, R. Manchek, and V. Sunderam, "Integrated PVM Framework Supports Heterogeneous Network Computing", Computers Phys. 7, 2 166-175 (1993).

7. C. D. Kellough, "Installation of Linux, PVM, and MCNP on Personal Computers." Los Alamos National Laboratory Research Note. XTM-RN (U) 96-008. (September 1996).

8. G. W. McKinney, "A Practical Guide to Using MCNP with PVM," Trans. Am. Nucl. Soc., 71, 397 (1994).

9. G. W. McKinney, "Parallel Processing Monte Carlo Radiation Transport Codes," Proceedings of the 8th ICRS, Arlington, Texas, April 24-28 (1994).

10. G. W. McKinney et al., "Multiprocessing MCNP on an IBM RS/6000 Cluster," Trans. Am. Nucl. Soc., 68, 212 (1993).

11. H. M. Abhold, J. S. Hendricks, "MCNP Quality Assurance Plan" LANL Research Report LA-13138 (April 1996).

12. J. D. Court, J. S. Hendricks, "Benchmark Analysis of MCNP EnDF/B-VI Iron," LANL Research Report LA-12884 (December 1994).

4. Investigation of Peak Dose Location Movement During Subject Irradiation and Dosimetry Effects.

The BNCT treatment planning procedure of the HARVARD/ MIT team relies on calculated dose rates to evaluate various epithermal neutron irradiation beam orientations. Often, one or more additional beams is used to increase the therapeutic ratio in deep parts of the tumor. These additional beams can be of equal or fractional effective time with the first beam, as indicated by its "weighting factor"[1]. Weighting factors, although strictly the ratio of any beam's neutron fluence to the first beam's fluence, can be thought of as the ratio of irradiation times, since the fluence rates are roughly constant with time. MacNCTPlan can then combine the dose rate distributions by multiplying a voxel's second beam dose rate by the second beams weighting factor and adding it to the first beam's dose rate to the same voxel. The best therapeutic ratio can be determined by changing the weighting factors of different combinations of beam orientations.

Using the final weighting factors and combination of all beams prescribed, the global maximum dose rate can then be determined in MacNCTPlan. The prescription dose could then divided by this dose rate to determine the neutron fluence, or effective irradiation time, delivered from beam one, although it is actually determined using phantom measurements, as described in chapter 2. Equation 4.1 states that the sum of the dose rates for the combined global maximum dose rate location, CGM, times their respective effective beam times is the prescription dose, D_p.

$$D_p = DR_{B1}^{CGM} \times t_{B1}^{Eff} + DR_{B2}^{CGM} \times t_{B2}^{Eff} + ...$$
<div style="text-align:right">Equation 4.1</div>

Since the beam weighting factor for beam i, w_i, is the ratio of t_{Bi} / t_{B1}, it can be substituted into Equation 4.1 for t_{Bi}, yielding equation 4.2.

$$\frac{D_p}{\left(DR_{B1}^{CGM} + DR_{B2}^{CGM} w_2 + ...\right)} = t_{B1}^{Eff}$$
<div style="text-align:right">Equation 4.2</div>

After the first beam's irradiation time is known, the others can be solved for using the weighting factors.

4.1 Identification

Occasionally it is necessary to end the first beam irradiation prior to the anticipated irradiation time due to subject discomfort or gradual misalignment with the irradiation beam. The second beam irradiation time is then increased to achieve the prescription dose. This changes the effective irradiation times, their ratios and the realized weighting factors. If the changes do not disrupt the location of the global maximum, the prescription dose can be achieved by increasing the second beam irradiation and adding the additional dose to the integrated global maximum dose. For combinations of low weighing factors, minimum beam shortening and certain beam orientations, this process would yield the correct dose.

If the duration of the second beam is increased near to that of the first beam, the location of the combined global maximum will move closer to the second beam's maximum dose rate location. When this shift takes place, the combined global maximum's dose rate will suddenly and dramatically increase, according to the beam's relative position. For parallel opposed beams, this would cause an order of magnitude increase in the dose rate as the CGM dose rate became the second beam's maximum dose rate. Failure to take this change into account by continuing to use the second beam's dose rate contribution to the global maximum will lead to a dose underestimation at EOI that rapidly increases as time increases. Fortunately, it is possible to predict when this change will take place and, in some cases, determine the new dose rates to the global maximum.

4.2 Explanation

As mentioned in chapter 2, there is a distinct change in the dosimetry perspective from dose rates to integral dose. In the treatment planning evaluation, dose rates from

different beams are combined using weighting factors. In effect, the beam irradiations are applied simultaneously. During the actual irradiation, however, the beams are applied sequentially. Dose rates vary significantly chronologically and spatially during the multiple beam irradiation.

During the first dose fraction, the isodose distribution is straightforward. The maximum dose rate occurs at the location determined solely that beam. Accordingly, the maximum dose is located at the maximum dose rate location (MDRL). The global maximum dose at the end of the first beam irradiation is the maximum dose rate multiplied by the effective time. After a brief delay for subject repositioning, the second fraction is delivered.

The second beam's dose distribution is a function of both the first and second beams, although the maximum dose rate (MDR) is now solely determined by the second beam. When the second beam is shorter than the first, the global maximum will remain in the vicinity of the first beam's MDRL. The second beam is contributing a small amount to the global maximum, the first beam's contribution to that point is significantly higher. When the second beam is roughly equal to the first, the global maximum will move in a manner related to the positioning of the two beams.

For roughly opposed beams, the global maximum will move to the opposite side of the head quickly. During this short transition time, it is possible for the global maximum to be at neither beam's maximum dose rate location. As the second beam's effective irradiation time becomes much longer than the first, the global maximum will move to the second beam's MDRL. The above process of global maximum movement during a nearly parallel opposed beam irradiation is shown in figure 4.1, which is the chronological dose reconstruction of one of the Harvard/MIT BNCT subjects, 96-4.

Figure 4.1 Subject 96-4 Chronological Dose Reconstruction. The solid line shows the dose to the first beam's maximum dose rate location. The dashed line shows the dose to the second beam's maximum dose rate location on the other side of the subject's head. The dots represent the highest cumulative dose, the global maximum, to any location within the subject's head.

Several important points are represented in figure 4.1. There are two plateaus in the graph indicating times the beam was turned off. Since there was no neutron or gamma fluence delivered, no dose was accumulated. The first plateau represents planned subject repositioning; the second was an unexpected interruption in the irradiation beam. Since the subject's head was reoriented to a nearly parallel opposed position with respect to the irradiation beam, the dose rates change significantly after the first repositioning. The movement of the global maximum is apparent near the end of irradiation. The duration of the transition time is not obvious in the above graph, but shown in the blow up of the region of interest, figure 4.2.

885

884

883

882

881

Dose (cGy)

880

879

878

877

876

875

——— Dose @ B1 MDRL

······· Dose @ B2 MDRL

● Global Max

404   405   406   407   408

Time After the Start of Irradiation (min)
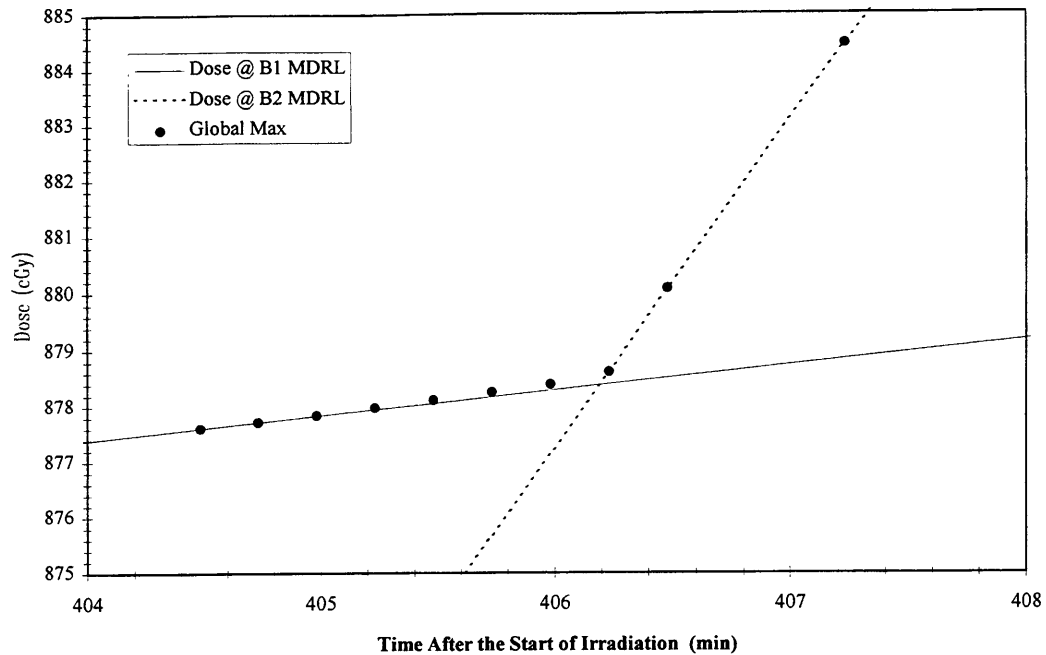
Figure 4.2. Enlargement of Figure 4.1. Near EOI. Fig 4.2 shows the enlarged region of fig 4.1 near the end of irradiation. Note the small time steps. The global maximum determined at 405.5, 405.7 and 405.9 minutes after the beginning of irradiation is not at either beam's maximum dose rate location.

In less than two minutes, the global maximum went through its transition period. After this time, the global maximum dose rate greatly increased from 0.40 RBE cGy/min to 5.57 RBE cGy/min. At the end of irradiation, the dose to the first beam's MDRL was 880 cGy, while the dose rate to the seconds beam's MDRL was 910 cGy. Five minutes after the transition period began, the irradiation was concluded. Since this movement was not anticipated, the online dosimetry used the same contribution of the second beam to the global maximum, plotted along the solid line in Fig 4.2. This incorrect assumption resulted in an overdose of 30 cGy, or 3.2 % of the final dose. Had the irradiation continued, the dose underestimation and resulting overdose would have become increasingly larger at a rate of 5.17 RBE cGy/min. Fortunately it is possible to calculate when this effect occurs, providing a time frame that the second beam should conclude, or dosimetry should be altered to account for the change.

For perpendicular beam orientations, the global maximum moves slowly. The global maximum's location is much more sensitive to small changes in the duration of the

second beam's irradiation time. The chronological dose reconstruction for subject 97-3 is shown below in Figure 4.3. and the expansion of the region of importance, in Figure 4.4.
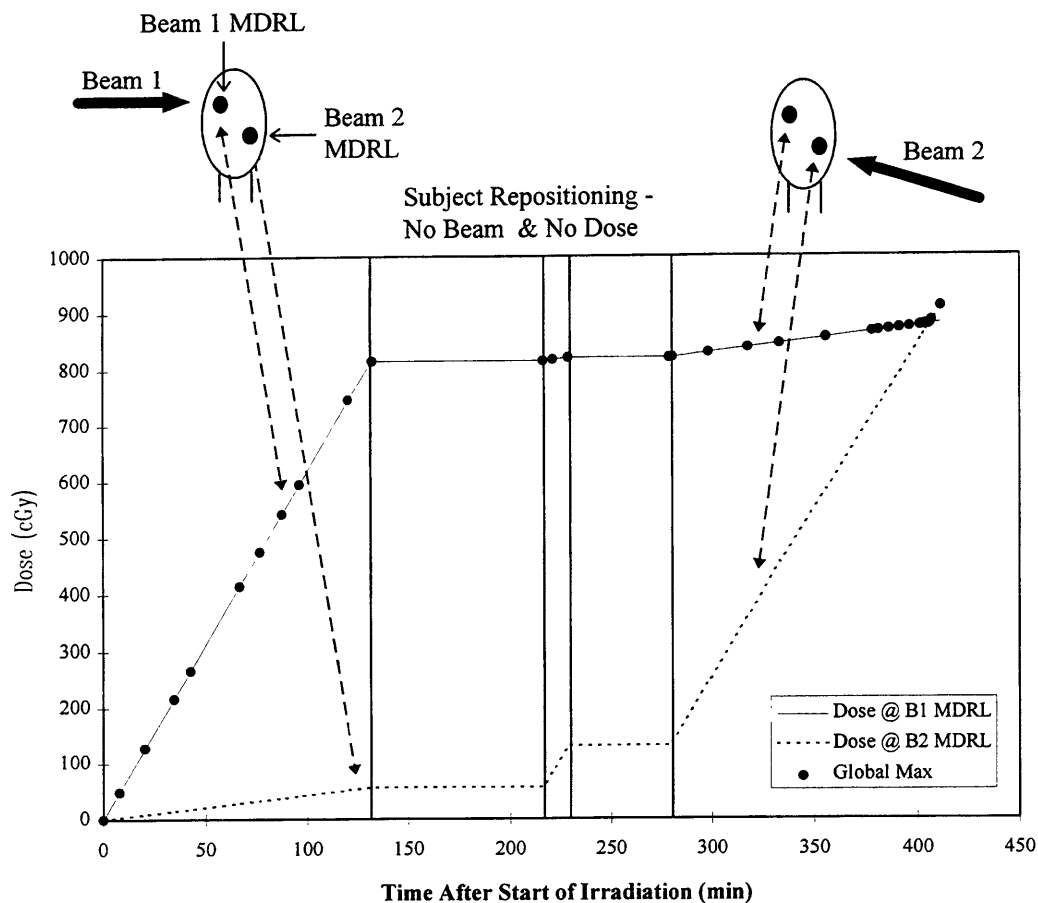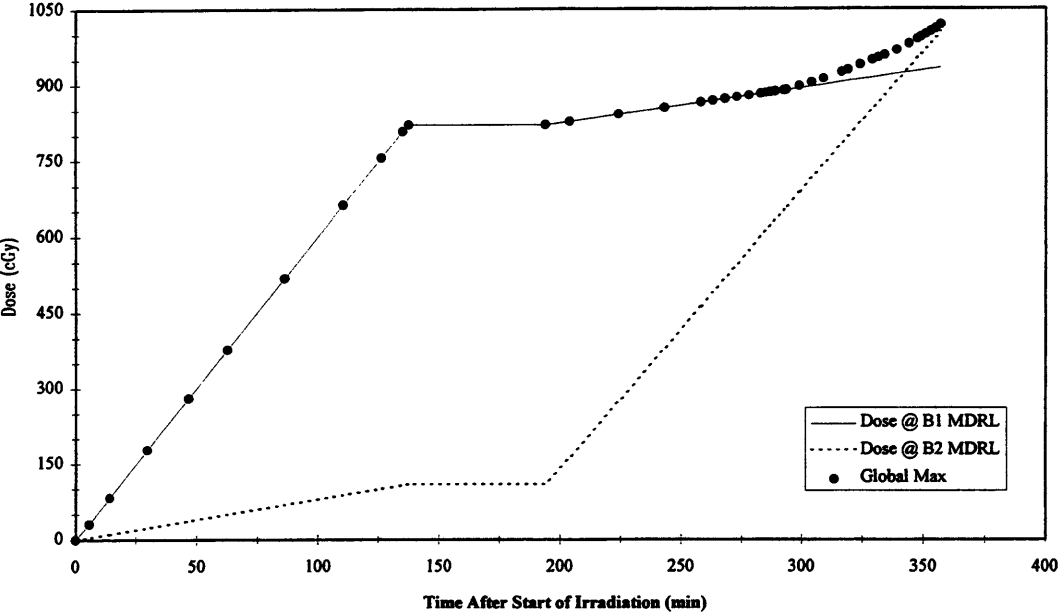

Figure 4.3 Subject 97-3 Chronological Dose Reconstruction. The solid line shows the dose to the first beam's maximum dose rate location. The dashed line shows the dose to the second beam's maximum dose rate location. The dots represent the highest cumulative dose to any location within the subject's head.
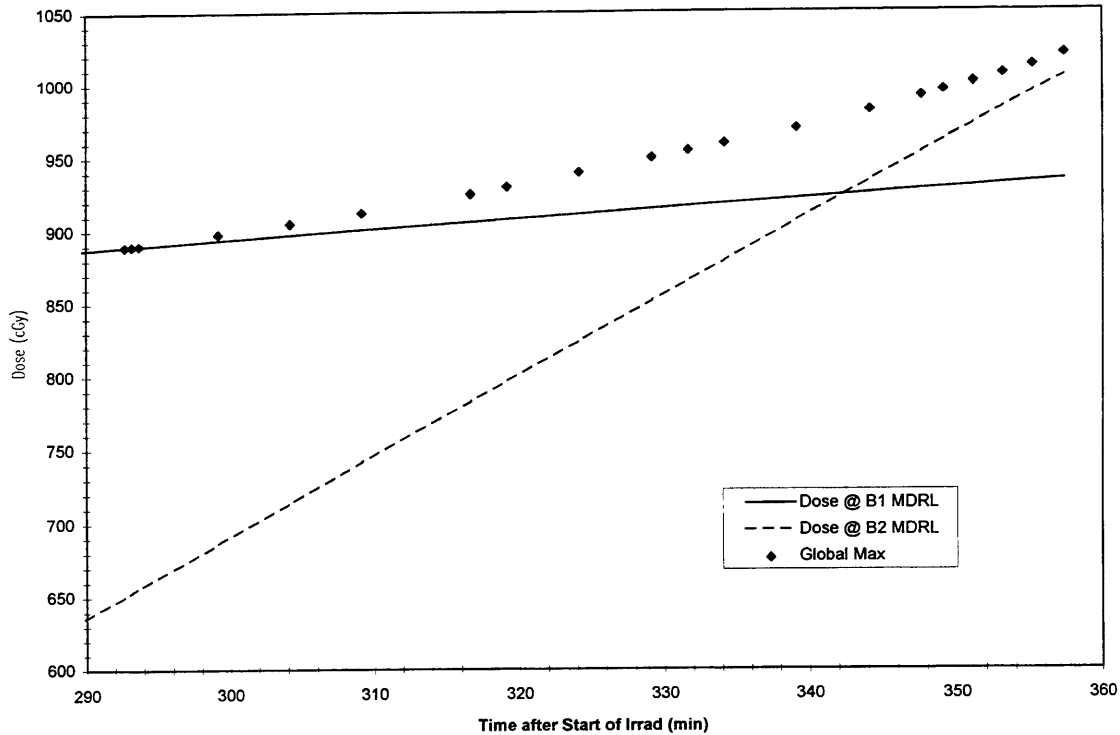
Figure 4.4 Enlargement of Figure 4.3 near EOI. Subj. 97-4 Chronological Dose Reconstruction.

Figures 4.3 and 4.4 indicate several important differences to the previous parallel opposed case. The first is the extended transition time, more than one hour in length, that the global maximum was not in either beam's maximum dose rate location. Had the irradiation continued, the transition time would have been much longer. Since the transition time is significant, the global maximum is much larger, on the order of fifty to seventy-five cGy, or five to eight percent, higher than the calculated dose at that time.

The difference between the parallel opposed and perpendicular beam irradiations and their respective global maximum movements is the three dimensional combination of their dose distributions. While the parallel opposed beams are essentially adding their chronological dose vs. depth profiles, the spatial and temporal dose distributions include the beam profile and scattering to a much higher degree. Thus it is possible for the dose distribution, which peaks at one or two cm from a single beam, to peak at deeper depths when multiple beams are applied in conjunction.

78

4.3 Prediction

Although it is difficult to predict when the transition begins or ends without full knowledge of the dose rates to all locations, it is possible to calculate a rough estimation easily for the parallel opposed cases, since the global maximum is almost always at one of the two beam's MDRL. For a two beam irradiation, only four doses are needed: each beam's dose rate contribution to each beam's maximum dose rate location. When the accumulated doses at both MDRL's are equal, the global maximum is either in transition, or simultaneously present in both locations. This "crossing over" condition, illustrated at 406.2 minutes after the beginning of irradiation in figure 4.2, is expressed mathematically by:

$$DR^{B1}_{B1\ MDRL} * T^{B1} + DR^{B2}_{B1\ MDRL} * T^{B2} = DR^{B1}_{B2\ MDRL} * T^{B1} + DR^{B2}_{B2\ MDRL} * T^{B2} \qquad \text{Equation 4.3}$$

Where DR is dose rate and T is time. The subscript indicates location, the superscript indicates fraction.

The duration of the second irradiation, T^{B2}, is the only unknown. Solving for it produces the following equation:

$$\frac{\left(DR^{B1}_{B1\ MDRL} - DR^{B1}_{B2\ MDRL}\right) * T^{B1}}{\left(DR^{B2}_{B2\ MDRL} - DR^{B2}_{B1\ MDRL}\right)} = T^{B2} \qquad \text{Equation 4.4}$$

Due to various contributions from the unequal boron concentrations in the second beam and geometric effects, the above factor will not be exactly one, but it should be close to it.

Exact determination of the global maximum movement time would require the appropriate boron concentrations, which are not known until after the irradiation is concluded. Fortunately, since the dose fraction to normal tissue from boron is ten to fifteen percent, dose assumptions of 12 ppm and 10 ppm produce reasonable estimations

for the time the global maximum would move. This insensitivity to boron concentrations means the transition times can be calculated at the beginning of the second beam irradiation, rather than during the transition time. Below is a table showing assumed boron concentrations for each beam and the resulting fliptime for 96-4.

Table 4.1 Flip times for Subject 96-4

Predicted Data		B1	B2	B1	B2	
B1 (ppm)	B2 (ppm)	B1 MDRL	B1 MDRL	B2 MDRL	B2 MDRL	Predicted Fliptime
15	10	6.556	0.478	0.443	6.330	133.7
12	10	6.401	0.478	0.442	6.330	129.6
15	8	6.556	0.476	0.443	6.207	136.5
12	8	6.401	0.476	0.442	6.207	132.4
10	8	6.247	0.476	0.440	6.207	129.7
15	6	6.556	0.475	0.443	6.084	139.5
12	6	6.401	0.475	0.442	6.084	135.3
10	6	6.247	0.475	0.440	6.084	132.5
Actual	Data					Actual Fliptime
11.980	8.094	6.369	0.476	0.441	6.213	132.2

Using reasonable approximations for the boron concentrations for each beam, a reasonable approximation can be made for the fliptime. The current assumptions of 12 and 10 ppm combined with a known beam 1 irradiation time of 128 min would have predicted a flip time of 129.7 min, within three minutes of the fliptime calculated using the actual biodistribution data.

A similar retrospective dosimetry analysis of all of the HARVARD/MIT two beam subjects indicates that the global maximum changed its location for three subjects, as shown in table 4.2 The ratio of each beam's dose rate to its dose rate at the global maximum dose rate is an indication of the CGM movement. If the ratio is unity, the

global maximum dose rate is in the same 1 cm^3 volume of space as a particular beam's maximum dose rate.

Table 4.2. Subject Dose Rate Contributions (DCR)

	Beam 1 (min)	Beam 2 (min)	Beam 1 DCR	Beam 2 DCR
97-3	132.54	157.03	0.2595	0.9003
97-2	164.69	50.70	0.9886	0.1980
97-1	129.99	126.24	1.0000	0.1000
96-2	132.57	138.23	1.0000	0.0774
96-4	128.02	137.33	0.0693	1.0000
96-3	115.45	139.17	0.0626	1.0000

The above table shows the duration of each beam and the MCNP dose rates and the ratio of each beam's dose at the MDRL to the dose at the global maximum. This parameter may also be used to gauge the volume dose.

Table 4.2 indicates several points. For three cases, 97-3, 96-4, and 96-3, the irradiation was stopped after the global maximum had moved to near the second beam's global maximum location. In another case, 97-2, the global maximum had started moving.

Whether the movement of the global maximum is the cause or not, there is a relation between the movement and the difference between the subject's dose at the end of irradiation and retrospective dosimetry. As shown in table 4.3, the three largest overdoses, as determined through retrospective dosimetry, were the three subjects in which this movement occurred. Although if the movement was the only factor, subject 96-4's dose error would be 3.25 %, indicating other factors, such as changes in the fitting of the biodistribution curve, influence this error.

Table 4.3 Subject's Dose Estimation

	Flip ?	Dose Error
97-3	yes	0.82%
97-2	no	0.39%
97-1	no	-1.68%
96-2	no	-0.62%
96-4	yes	1.16%
96-3	yes	3.23%

The dose error is the difference between retrospective dose and the laptop dose at EOI.

4.4 Chapter Summary

The sequential application of beams will create dynamic dose rates, possibly changing the location of the global maximum. A retrospective analysis of the BNCT two beam subjects shows that the global maximum did move to near the second beam's MDRL in three cases. This movement may explain why these three subjects have the three largest overdoses of all the two fraction subjects, although other factors, such as an incomplete biodistribution curve, will also affect the dose calculated at the end of irradiation. To prevent these overdoses from occurring in the future, it is possible to calculate when the increase in dose rates will occur. If the second beam irradiation exceeds this time, the contributions of each beam's maximum to the global maximum should be determined.

References

1. W.S. Kiger III, "MacNCTPlan user's manual" Version 2.1. Harvard/MIT BNCT Project internal document (1998).

2. W. S. Kiger III, "BNCT Rx manual dosimetry protocol," Harvard/MIT BNCT Project internal document (1997).

5. Retrospective Volume Dosimetry Calculations and Effects

Dose volume histograms (DVHs) are important to the medical physicist and radiation oncologist to determine the therapeutic advantage of the irradiation and to help relate physical effects with dose distributions[1,2]. The DVH is a plot of how much volume of tissue receives a specific dose. A specific point indicates that a certain volume has received the corresponding amount of dose or higher. The DVHs for the Harvard/M.I.T. MIT subjects can be easily calculated from the dose rates for each voxel, the effective beam irradiation time, and effective boron concentration. The total dose per voxel can also be used to calculate the volume averaged dose, another useful value to the radiation oncologist. An analysis of the volume doses lead to a proposed alternative subject grouping.

5.1 DVH Calculation

The DVH calculation process is fairly straightforward. The medical physicist defines the region of interest for neural tissue within MacNCTPlan, just as he did for tumor. A neural tissue materials file is generated. From within Excel, or other spread sheet program, each voxel's material is correlated with its total RBE dose, as defined by the total effective irradiation times and effective boron concentrations for each beam. Since the fraction of neural tissue is known for each material from the materials file, the neural tissue volume corresponding to each dose is known. Since MacNCTPlan only identifies the volume fraction of the ROI in increments of twenty percent[3], there are only five volumes associated with each material and hence dose: 0.2 cm^3, 0.4 cm^3, 0.6 cm^3, 0.8 cm^3 and 1 cm^3. For convenience, voxel doses are grouped into 50 cGy dose bins. Using the Excel histogram data analysis tool, the number of doses in each of the 50 cGy bins is determined for each of the five fractions. This number is then multiplied by the corresponding volume contribution for each dose bin to find the total volume associated with each dose bin. The DVH is the cumulative volume associated with each bin

subtracted from the total volume. An example spread sheet DVH calculation is shown in Table 5.1.

Table 5.1 DVH Spread Sheet for Subject 97-2.

100% tissue voxel dose	80% tissue voxel dose	60% tissue voxel dose	40% tissue voxel dose	20% tissue voxel dose	Dose Bins	# 100% tissue voxels	# 80% tissue voxels	# 60% tissue voxels	# 40% tissue voxels	# 20% tissue voxels	Dose Bin Vol.	Int. Bin Vol.	**DVH**
479	438	365	414	522	**50**	0	0	0	0	0	0	0	**1487.6**
529	527	389	458	365	**100**	0	1	0	4	7	3.8	3.8	**1483.8**
578	293	426	494	400	**150**	83	42	72	27	32	177	180.8	**1306.8**
410	752	455	524	443	**200**	128	54	66	26	18	224.8	405.6	**1082**
462	781	280	554	357	**250**	113	46	57	15	17	193.4	599	**888.6**
501	824	304	323	209	**300**	97	37	47	26	11	167.4	766.4	**721.2**
322	595	335	213	234	**350**	77	30	37	22	11	134.2	900.6	**587**
355	531	365	297	263	**400**	74	19	35	14	14	118.6	1019.2	**468.4**
392	476	243	509	717	**450**	61	17	25	15	8	97.2	1116.4	**371.2**
428	156	262	567	739	**500**	59	12	17	8	3	82.6	1199	**288.6**
467	339	294	593	755	**550**	39	12	11	8	10	60.4	1259.4	**228.2**
255	773	322	263	637	**600**	35	7	9	7	4	49.6	1309	**178.6**
281	827	231	235	663	**650**	28	10	6	3	7	42.2	1351.2	**136.4**
309	760	262	197	308	**700**	31	6	4	2	4	39.8	1391	**96.6**
342	200	556	361	334	**750**	23	4	3	2	6	30	1421	**66.6**
373	180	616	407	372	**800**	14	9	3	1	6	24.6	1445.6	**42**
413	160	658	169	177	**850**	11	7	3	2	5	20.2	1465.8	**21.8**
218	875	611	187	342	**900**	6	6	3	4	3	14.8	1480.6	**7**
244	605	506	211	377	**950**	1	2	2	2	9	6.4	1487	**0.6**
269	463	441	239	151	**1000**	0	0	0	1	1	0.6	1487.6	**0**
297	320	393	275	645	**1050**	0	0	0	0	0	0	1487.6	**0**
332	126	435	335	868	**1100**	0	0	0	0	0	0	1487.6	**0**
370	287	171	709	400	**1150**	0	0	0	0	0	0	1487.6	**0**
192	330	302	926	443	**1200**	0	0	0	0	0	0	1487.6	**0**
218	366	713	952	777	**1250**	0	0	0	0	0	0	1487.6	**0**
235	733	760	424	768									
259	766	828	290	206	Sum	880	321	400	189	176	1487.6		
296	823	748	431	185									

The two bolded columns, dose bins and DVH, form the DVH plot. The five left most columns are an incomplete listing of all the voxel doses of a particular volume fraction.

Although it is possible to calculate the DVH without using dose bins, it is not possible to plot with Excel. While other available plotting packages can plot the exact DVH, that amount of precision is not necessary.

5.2 Dose Volume Histogram Results

Figure 5.1 shows the dose volume histograms for the ten most recent Harvard/MIT BNCT subjects.

	Subject	Initials	Prescription Dose	Vol Averaged Tissue Dose	Peak Tissue Dose
	97 - 7	J.T.	1065	303	1088
	97 - 6	C.M.	1065	296	1105
	97 - 4	G.R.	1065	318	1153
	97 - 3	G.C.	970	424	983
	97 - 2	T.T.	970	343	992
	97 - 1	N.M.	970	419	954
	97 - 5	I.R.	1065*	275	909
	96 - 4	J.L.	880	448	891
	96 - 3	G.M.	880	474	908
	96 - 2	S.J.	880	511	875
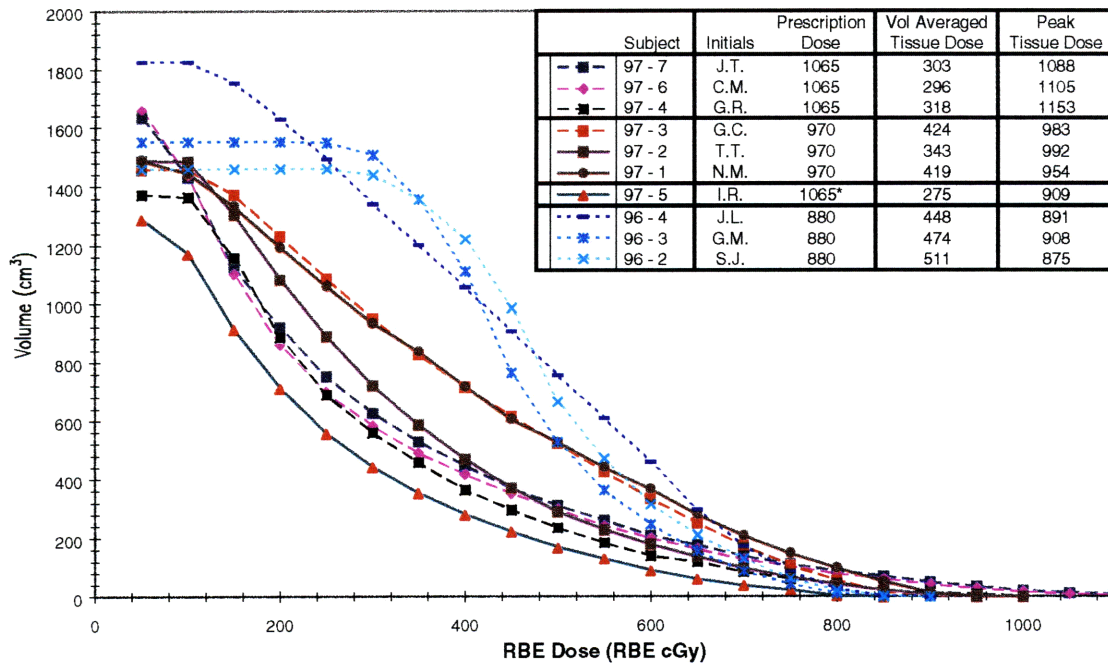
Figure 5.1 Subject Brain Tissue Dose Volume Histograms

Since the DVH curve is integral dose, the y intercept shows the volume that receives zero dose or above, i.e. all brain tissue. The calculated volumes could then be compared to known average data. According to ICRP, the average volume of tissue is 1355 and 1220 for males and females respectively, based on average density and masses[4]. A more recent head model[5,6], adopted by the MIRD committee as a standard for internal dose calculations, gives a brain tissue volume of 1467.6 cm^3, in agreement with the calculated volumes obtained here.

The curves show two distinct effects. The low dose regions have dramatic differences in slopes, which are prescription dose independent but dependent on beam geometry. The curves for subjects 96-3 and 96-2 even show a plateau region, which results from the greater volume

doses received from a parallel opposed irradiation. The subjects 97-7, 97-6, 97-5, 97-4, were all single beam irradiations and show the lowest DVHs in the low dose region.

Unlike the low dose region, the high dose region of the DVH is dependent on the magnitude of the peak dose, as expected. The high dose region is shown below in Fig 5.2

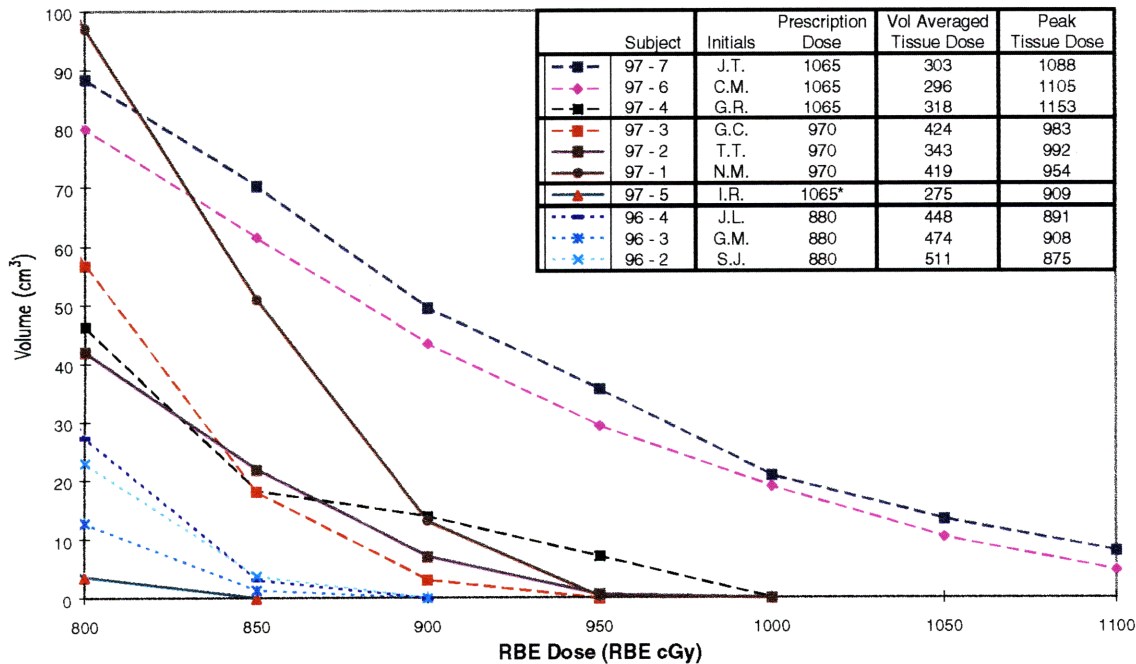|	Subject	Initials	Prescription Dose	Vol Averaged Tissue Dose	Peak Tissue Dose
–■–	97 - 7	J.T.	1065	303	1088
–◆–	97 - 6	C.M.	1065	296	1105
–■–	97 - 4	G.R.	1065	318	1153
–■–	97 - 3	G.C.	970	424	983
–■–	97 - 2	T.T.	970	343	992
–●–	97 - 1	N.M.	970	419	954
–▲–	97 - 5	I.R.	1065*	275	909
···●···	96 - 4	J.L.	880	448	891
···✳···	96 - 3	G.M.	880	474	908
···✕···	96 - 2	S.J.	880	511	875

Figure 5.2 Higher Dose Region DVH

Although it appears that there are volumes of tissue that receive higher than the prescription dose, this is incorrect. The scaling factors that adjust the MCNP calculations to experimental data were altered to fit these two cases separately. The highest dose is always the prescription dose, wherever it is located, and is the x intercept of the DVH curve.

Dose volume histograms can also be generated for the tumors. The method used to generate neural tissue DVHs, where nearly a thousand cells contribute to the volume dose could be used, but tumor DVHs can have as few as ten to twenty contributing cells. In this case, the DVH curve is plotted in response to each individual voxel, rather than a dose bin grouping of voxels. RBE tumor dose is found for each cell. The doses are then sorted from lowest to highest and the integral volume is found for each cell, as shown in Table 5.2.

Table 5.2 Example Spread Sheet for Tumor DVH Calculation

Voxel Tumor Dose	Voxel Tumor Fraction	DVH
2343	0.6	0.6
2302	1	1.6
2280	0.4	2
2237	0.6	2.6
2193	0.2	2.8
2184	0.2	3
2174	0.6	3.6
2149	0.4	4
2130	0.2	4.2
2119	1	5.2
2103	0.2	5.4
2075	0.2	5.6
2050	0.6	6.2
2017	0.6	6.8
1991	0.2	7
1973	0.2	7.2

The above table is a complete listing of all voxels containing a tumor fraction of 20% or more.

The corresponding plot to the data shown in Table 5.2, as well as other Harvard/MIT BNCT subjects, is shown in Figure 5.3.

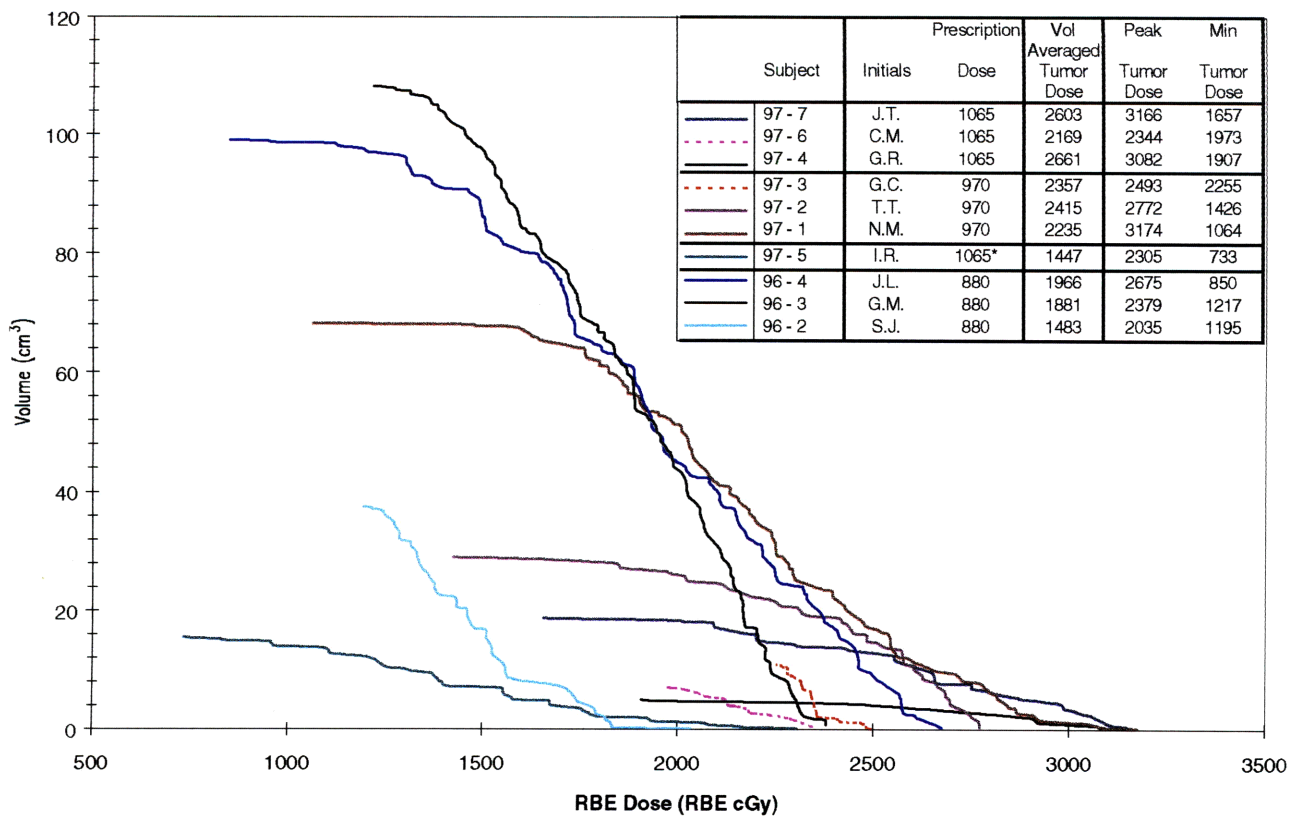|	Subject	Initials	Prescription Dose	Vol Averaged Tumor Dose	Peak Tumor Dose	Min Tumor Dose
	97 - 7	J.T.	1065	2603	3166	1657
	97 - 6	C.M.	1065	2169	2344	1973
	97 - 4	G.R.	1065	2661	3082	1907
	97 - 3	G.C.	970	2357	2493	2255
	97 - 2	T.T.	970	2415	2772	1426
	97 - 1	N.M.	970	2235	3174	1064
	97 - 5	I.R.	1065*	1447	2305	733
	96 - 4	J.L.	880	1966	2675	850
	96 - 3	G.M.	880	1881	2379	1217
	96 - 2	S.J.	880	1483	2035	1195

Figure 5.3 Tumor Dose Volume Histogram

Figure 5.3 shows a variety of effects on the tumor DVH. In addition to beam geometry effects, the tumor location and extent must be also be considered. Ideally, all of the tumor would be in a dose region greater than 3000 RBE cGy[7]. Since the tumors vary in size, location and extent, the beam geometry and dose cohort have varying effects. Surface tumors will have high peak and minimum tumor doses, while large tumors could have high peak tumor doses, but low minimum tumor doses. The peak and minimum tissue and tumor doses are shown the legends of Figures 5.1, 5.2 and 5.3. The volume averaged dose will be described in section 5.3.

There is a large difference between the tumor DVH and the neural tissue DVH, due to the increased dose to tumor cells. This increase is caused by the increased concentration of BPA in tumor cells, by a factor of 3.5 times that of normal tissue. The RBE of boron dose is increased to 3.8 for tumor from 1.35 for normal tissue. When the tumor and tissue DVH are combined, the therapeutic advantage is shown more clearly, as indicated by the arrow in Figure 5.4.
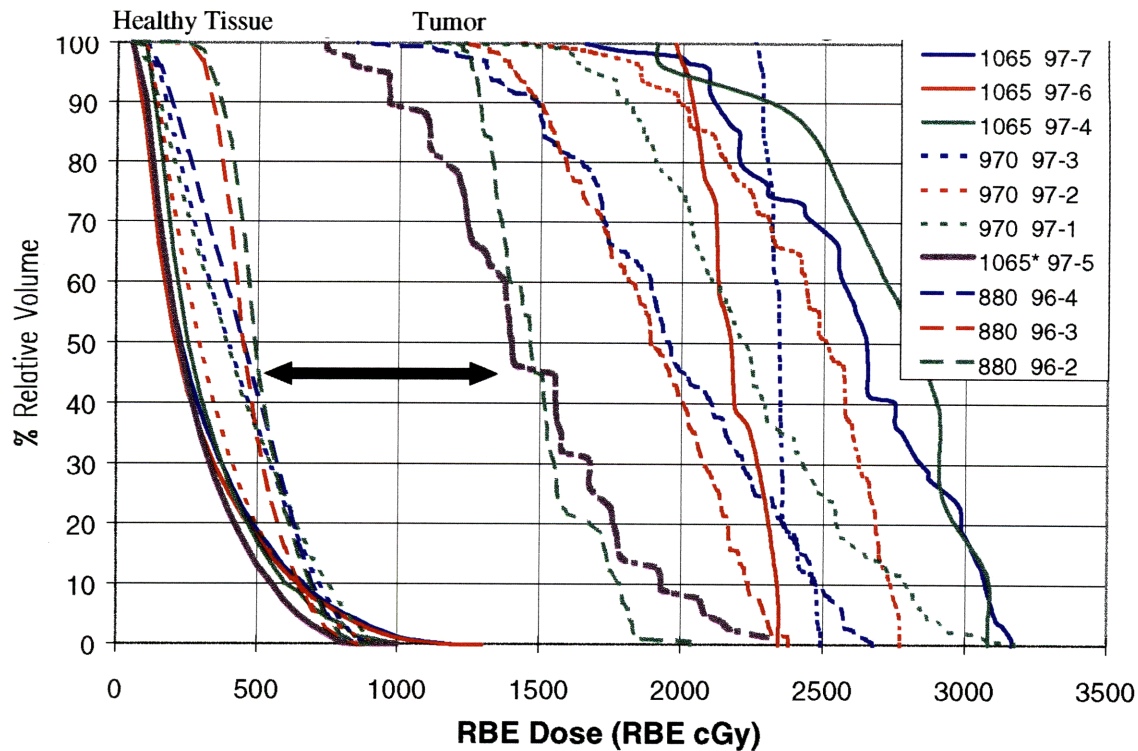
Figure 5.4 Tumor and Tissue DVHs. All volumes are expressed in terms of their relative percentage.

5.3 Volume Averaged Dose

Another clinically important value is the volume averaged dose. Both the tumor and brain volume dose can be calculated as the sum of all tumor or brain voxel doses, D(i), times their associated tumor or brain volume, V(i), divided by the total tumor or brain volume, as shown in Equation 5.1

$$\text{Volume Average Dose} = \frac{\sum_{i=1}^{i=11025} D(i) \cdot V(i)}{\sum_{i=1}^{i=11025} V(i)} \qquad \text{Equation 5.2}$$

While equation 5.2 is a sum over all voxels, only one to two thousand voxels have non zero volume fractions of brain. Typically one hundred voxels have non zero volume fractions of tumor.

Using equation 5.2, the volume averaged tumor and tissue doses were calculated for the Harvard / M.I.T. BNCT subjects, listed in figures 5.1, 5.2 and 5.3.

5.4 Relation to Peak Dose

For all of the above subjects, except 97-4 and 97-5, two beams were used. The second beam, in addition to making a contribution to the global maximum, increases the volume dose. One measure of how the beams combine is the ratio of the dose at a particular beam's maximum to the dose at the global maximum. For example, if two beams of equal irradiation times are very close, the global maximum would be in the vicinity of each beam's maximum, and the above ratio would be very close to unity, as illustrated in figure 5.5.

Beam 1　　　　　　　Beam 2

Beam 1 MDL　　　　　　Beam 2 MDL

Post Irradiation Global Max
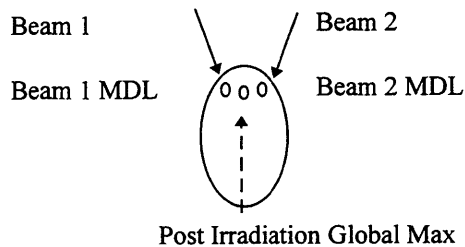
Figure 5.5 Dual Irradiation with close entry locations.

In this case, only small volumes of tissue would receive high doses when the global maximum reaches the prescription dose. For nearly opposed beams, the global maximum will be close to either beam's maximum, which are widely separated, as shown in figure 5.6. Thus one ratio would be close to unity and the other will be close to zero.

Locations of the Maximum
Dose from Individual Beams
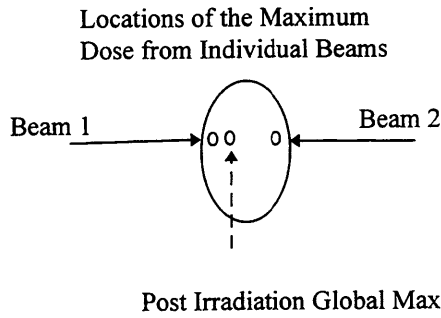

Post Irradiation Global Max

Figure 5.6 Dual Beam Irradiation with distant entry locations.

Since the second beam is depositing more of its energy in the region of its maximum, rather than the global maximum, much larger volumes receive a higher dose. This effect can be seen in the above DVH for doses ranging from 200 to 650 cGy. The subjects' maximum dose ratios are shown in table 5.3, sorted by decreasing value of the second beams contribution.

Table 5.3 Subject Max Dose Ratios

	Beam 1	Beam 2
97-3	0.2595	0.9003
97-2	0.9886	0.1980
97-1	1.0000	0.1000
96-4	0.0693	1.0000
96-3	0.0626	1.0000
97-5	1	-
97-4	1	-

According to the above chart, 96-4 and 97-1 should have similar high dose curves, and 97-3 and 97-2. 97-1 should be between those two groups. Unfortunately, only 96-4 and 97-1 grouping are correct.

5.5 Proposed Grouping

If the volume averaged tissue dose is considered to be the representative quantity for a dose cohort group, rather than the peak dose, a new grouping results. While the cohort groups will still be defined in accordance to the peak tissue dose, as required by

the protocol, this new grouping provides an alternative way to evaluate the data. The proposed groupings are listed in table 5.4, while the subject volume doses are plotted in Figure 5.5

Table 5.4 Proposed Subject Dose Cohorts

BNCT Subject	Vol Averaged Tissue Dose RBE cGy	4 Proposed Groups			2 Proposed Groups		
		Group Avg RBE cGy	Deviation RBE cGy	% Increase	Group Avg RBE cGy	Deviation RBE cGy	% Increase
96 - 2	511	493	25.7	14.4			
96 - 3	474						
96 - 4	448				455	37.9	48.3
97 - 3	424	431	15.6	30.3			
97 - 1	419						
97 - 2	343	331	17.2	13.4			
97 - 4	318						
97 - 7	303				307	25.2	
97 - 6	296	291	14.3				
97 - 5	275						

The two proposed grouping methods, with group average doses and the amount of increase between groups.
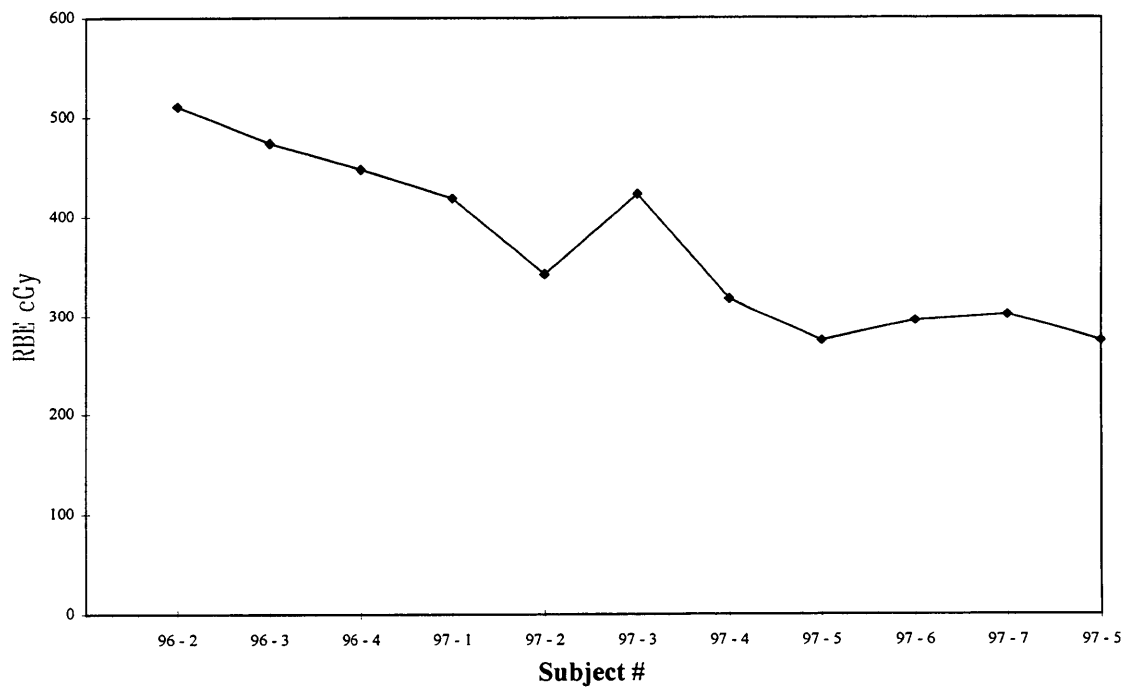

Figure 5.7 Subject Volume Doses

Figure 5.7 illustrates an important point. Even though the peak dose increases with increasing subject number, the volume doses can decrease. The recent subjects have been treated with single beam applications which have lower volume doses than the dual beam irradiations.

5.6 Peak Tissue Dose vs. Peak Brain Dose

The final value of possible clinical significance calculated for this thesis is the peak brain dose. This value is important when comparing data to other BNCT clinical trials. While the peak dose to tissue is a calculation based on phantom measurements, its location is not measured when multiple irradiation beams are applied. Using the calculated voxel doses, the peak dose to any voxel containing 20% or more neutral tissue or tumor can be found. The peak tissue, brain and tumor doses for the Harvard/MIT subjects are shown in Table 5.5.

Table 5.5 Peak Doses to Various Tissues

Subject	Prescription Dose	Peak Tissue Dose	Peak Neural Tissue Dose	Peak Tumor Dose
97 - 7	1065	1088	1020	3166
97 - 6	1065	1105	1042	2344
97 - 4	1065	1153	989	3082
97 - 3	970	983	933	2493
97 - 2	970	992	830	2772
97 - 1	970	959	959	3174
97 - 5	1065*	909	830	2305
96 - 4	880	891	889	2675
96 - 3	880	908	843	2379
96 - 2	880	875	875	2035

Subject 97-5 was originally placed in the 1065 prescription dose cohort, but the second irradiation beam was not completed.

References

1. G. J. Kutcher, "Quantitative Plan Evaluation," *Advances in Radiation Oncology Physics: Dosimetry, Treatment Planning and Brachytherapy*, edited by J. P. Purdy, no. 15, 998 (1992).

2. Benedick Fraass, "Clinical Applications of 3-D treatment Planning," *Advances in Radiation Oncology Physics: Dosimetry, Treatment Planning and Brachytherapy*, edited by J. P. Purdy, no. 15, 967 (1992).

3. W.S. Kiger III. "MacNCTPlan: user's manual," Harvard/MIT BNCT Project internal document (1998).

4. ICRP Report 23, "Report of the Task Group on Reference Man," ICRP Publication 23 (Pergamon Press, New York, 1975) .

5. L. G. Bouchet, W. E. Bolch, D. A. Weber, H. L.Atkins, and J. W. Poston Sr. "A revised dosimetric model of the adult head and brain", J. Nucl. Med.; **37**,7, 1226-36 (1996).

6. L. G. Bouchet, W. E. Bolch, D. A. Weber, H. L.Atkins, and J. W. Poston Sr. "MIRD Pamphlet No. 15: Radionuclide S Values in a Revised Dosimetric Model of the Adult Head and Brain".

7.G. E. Laramore, F. J. Wheeler, D. E. Wessol, K. J. Stelzer, T. W. Griffin. "A tumor control curve for malignant gliomas derived from fast neutron radiotherapy data: implications for treatment delivery and compound selection, " *Advances in Neutron Capture Therapy: Volume II, Chemistry and Biology*," edited by B. Larsson, J. Crawford and R. Weinreich. (1997).

6. Conclusions

This thesis contains improvements to the Harvard/MIT BNCT treatment process in three distinct areas. The treatment planning calculations were reduced in time, the dosimetry procedure during irradiation was increased in accuracy, and the retrospective volume dosimetry was calculated. A summary of the current steps in treatment and treatment planning is included.

As a result of this thesis work, the Harvard/MIT BNCT treatment planning calculations were considerably reduced, from two hours thirty minutes to fifty nine minutes for a single beam scoping calculation. This wall clock runtime reduction is from enhancements to the Monte Carlo program, MCNP4B, and utilization of parallel calculations (i.e. PVM) on a network of linked computers. A voxel dose rate analysis was performed to see if the run times could be lowered by running fewer particles, but it indicated that an appropriate number of particles were currently being run.

While the decrease in runtimes for a single beam is significant, typically the dose rates for four or five irradiation beams are calculated. A brief investigation into the total runtime reduction of all five beams showed that until the number of linked computers exceeds the number of potential beams, these calculations should not be performed in parallel. While PVM is not immediately applicable for these treatment planning calculations on two computers, the anticipated purchase of several high end computers will use this technology to reduce the calculation time to minutes, allowing the iterative approach currently used in conventional radiotherapy to be used.

During this thesis research, the previously unnoticed phenomenon of peak dose location movement was recognized and investigated. This movement has a direct effect on the calculations that determine the delivered peak dose to the subject during irradiation, creating the possibility of underestimation of peak dose, thus subject overdose. While the investigated cases had less than 5% overdose, the potential exists for

higher overdoses. For beams that are parallel opposed, this movement would cause a tenfold increase in dose rate to the peak dose location. Further investigation led to a prediction of when this movement would occur, and how to avoid its potential overdoses.

The calculation of volumetric dosimetry is useful for the radiation oncologist to relate the radiation damage and dose. The dose volume histograms, volume averaged dose, peak and minimum dose to soft tissue, brain tissue, and tumor were calculated. The DVHs illustrate the how different beam orientations and combinations can affect the dose distributions. Based on the volume averaged doses, an alternative subject grouping was proposed.

Appendix A

Appendix A includes a description of the failed attempts to install MCNP and PVM on various operating systems.

A.1 Windows

The operating systems Microsoft Windows NT and Microsoft Windows 95 are popular operating systems used on PC's. Adapting MCNP4B for use with PVM on these systems would greatly increase the number of computers available for addition to the parallel virtual machine, with minimal effort to reconfigure the system. Running MCNP in parallel on these systems had not been attempted previously.

Several problems were initially encountered. MCNP is a complex program requiring a well written compiler to create an executable that will pass the test suite. Lahey makes two such compilers, FORTRAN 77 (F77) and FORTRAN 90 (F90). The Lahey FORTRAN 77 was officially supported for the release of MCNP4A. FORTRAN 90 was tested and found to create an executable that is about ten percent faster than the executable created by Lahey F77.

Incorporation of the PVM libraries required a linker that would be able to read both the F77 object code and the PVM libraries, created by Microsoft C++. The Lahey and Microsoft object files and libraries were incompatible. Either PVM or MCNP would have to switch to a compatible compiler. Several tests were performed to identify compatible compilers. Three were found, although others may exist: Watcom C++ and Watcom FORTRAN, Microsoft FORTRAN Powerstation and Microsoft Visual C++, and Lahey FORTRAN and Metaware High C. Watcom FORTRAN would not compile the MCNP source code without extensive modifications. During testing, Microsoft FORTRAN Powerstation was acquired by Digital Equipment Corp., (DEC), who began offering their DEC Visual FORTRAN for Windows. It was able to compile MCNP with minor revisions because MCNP had already been ported to DEC operating systems,

which use a similar DEC compiler. The DEC FORTRAN linker was able to read the PVM libraries, and create a parallel version of MCNP, mcnp.pvm.

PVM for windows was installed in a similar manner as on Linux. Networked NT computers were linked together and successfully ran the PVM test executable "hello". Mcnp.pvm would start on other linked NT's, but they would not run.

A.2 MkLinux

In addition to the work on PC's, the linking of Macintosh computers to the virtual machine was investigated. The treatment planning software, MacNCTPlan is used on Power Macintosh computer, which would be convenient to link. Apple Computer ported the Linux kernel, called MkLinux for its Power Macintosh computers, making it exceptionally easy to install. Another port of Linux for Macintosh is Linux-pmac, supposedly faster than Apple's MkLinux, but more complicated to install.

The installation of MkLinux is handled by a Mac program, InstallMkLinux, which guides the user step by step through reconfiguring the system and installing MkLinux. The MkLinux operating system is well integrated with MacOS, providing a simple "boot MkLinux" button when the system starts. The most challenging part of the MkLinux installation, and any other Linux installation, was repartitioning the hard drive to create 500 megabytes or more of free space. After this was done with the program, pdisk, provided with InstallMkLinux, the computer was rebooted.

MkLinux was able to recognize all SCSI devices, including the SCSI CDROM, which allowed convenient installation of MCNP. Apple's MkLinux release also included the FORTRAN and C compilers, GNU G77 and GNU GCC, necessary to compile MCNP. Following the same procedure used for installing MCNP on a Linux computer, MCNP was compiled and linked on MkLinux. The test suite indicated several rounding errors, considered acceptable, and two tracking errors. The tracking errors indicate potential problems with the compiler or operating system. MCNPBNCT was able to run a BNCT treatment planning problem, but since this run was too slow to be useful, its

results were not verified. One of the main drawbacks of the MkLinux installation was the failure of its networking capabilities.

A.3 Linux-pmac

Another Linux based operating system, Linux-pmac, which had functional networking utilities, was installed on the same machine. Linux-pmac installation is conveniently managed by Red Hat, so once a simple boot disk is created, Linux-pmac can be installed via ftp. Although Linux-pmac's GNU G77 could not compile MCNP4B, it did recognize and execute the MkLinux MCNPBNCT executable. It also supported full networking capabilities.

From within the Linux-pmac operating system, PVM was obtained via ftp and installed. The Linux-pmac GNU GCC did compile PVM and the associated libraries. The computer was added to a virtual machine consisting of the Sager laptop and an MIT SGI Indigo computer. The PVM hello program worked appropriately, indicating the functionality of the virtual machine. MCNP was recompiled and linked with the PVM libraries in MkLinux to create "mcnp.pvm". Although the master MCNP executable was able to start subtasks on the Linux-pmac machine, they did not continue running. The Linux-pmac job running MCNP in parallel, like the Windows job, was unable to successfully complete.

A.4 Other Possibilities

Although none of the above trials was successful, several other options do exist. The GNU tools have been ported to the Windows operating systems, possibly allowing an installation similar to that of Linux. Other Linux and UNIX operating systems exist for the Macintosh, such as the Mach-Ten UNIX emulator. Additionally, all of these programs are occasionally upgraded, perhaps correcting some of the deficiencies encountered.